EFFECTS OF GEOMETRIC VARIATION AND RESIDUAL STRESS ON THE

DYNAMIC RESPONSE OF MULTILAYERD THIN MEMBRANE STRUCTURES

By

TAI CHUN HAN

A thesis submitted in partial fulfillment of
the requirements for the degree of

MASTER OF SCIENCE

WASHINGTON STATE UNIVERSITY
School of Mechanical and Materials Engineering

July 2007

To the Faculty of Washington State University:

       The members of the Committee appointed to examine the thesis of TAI CHUN HAN find it satisfactory and recommend that it be accepted.

_____
Chair

_____

_____

ACKNOLEDGEMENT

I would like to extend my thanks and appreciation to Dr. Jow-Lian Ding for providing the opportunity for me to work on this project, and for his persistent guidance over the course of this research. Dr. Ding was my advisor since my undergraduate year. He has been always encouraging and providing guidance in my academic career and making a difference of my life. Without him, this master degree is not possible. In addition, I would like to thank the committee members Dr. Amit Bandyopadhyay and Dr. Susmita Bose for their advises to my research and the summer support in 2006.

I would also like to thank my fellow lab mate Hngsoo for sharing with me his experience on pMUT fabrication and FEA code development, and providing many valuable guidance and help throughout my research work.

I would also like to thank my friends at Washington State University who have encouraged me throughout my undergraduate and graduate studies. In the end, I want to offer the greatest appreciation to my parents.

EFFECTS OF GEOMETRIC VARIATION AND RESIDUAL STRESS ON THE
DYNAMIC RESPONSE OF MULTILAYERD THIN MEMBRANE STRUCTURES

Abstract

By Tai Chun Han, M.S.
Washington State University
August 2007

Chair: Ding, Jow-Lian

Thin-film structures have found a wide variety of applications in emerging
technologies. Along with the hardware development, there is also a need for a design
methodology for such structure. The methodology would allow the designer to be able to
predict the performance of these structures before they are fabricated. The currently
available methodology assumes that the membrane structures are flat and all the
dimensions can be precisely measured. However, in reality, there are always some
variations on the dimension measurements. Furthermore, the structures usually have
somewhat distorted shapes due the residual stress introduced during the fabrication
process.

The objective of the current study was to gain insights into the dynamic responses
of thin membrane structures. Specifically, the effects of dimensional variations and shape
changes due to residual stress on the fundamental frequencies of the structures were
examined. The approach used was numerical simulation with ANSYS.

It was found that the increase of thickness and decrease of in-plane dimensions
would increase the resonance frequencies. However, a 15% variation of these dimensions
as deemed reasonable from the practical point of view still could not bring up the
predicted frequencies within the experimentally observed range. For the effects of shape

change, it was found that the domed shape has the highest frequency compared to other shapes with the same size and out-of-plane displacement, but multiple curvatures. To get a correlation between the shape change and residual stress, thermal cycling simulation was also performed. In this simulation, the structure was subjected to 25-1000-25 $^\circ$ C thermal cycling and the resultant deformed shape was then used as an input for the subsequent dynamic analysis. It was found that the deformed shape obtained from thermal cycling simulation would still underestimate the frequencies quite significantly. However, with a combination of dimensional variation and shape change, the predicted frequencies could be brought into closer to the experimentally observed values.

It was concluded that dimensional variation and shape change due to residual stress could significantly vary the dynamic response of the thin membrane structures. However, the quantitative evaluation of the contribution from residual stress requires further study on the source and realistic simulation of residual stresses.

TABLE OF CONTENTS

LIST OF TABLES

LIST OF FIGURES

Dedication

This thesis is dedicated to the almighty God,
the creator of heaven and earth,
the Alpha and Omega.

Nomenclature

E   Young's Modulus Gpa

v   Possion Ration

α Thermal Expansion Coefficent $10^{-6}/K^{\circ}$

$\sigma_{(yp)}$ Yield Stress MPa

ε Strain (in/in)

ρ Density Kg/M^{3}

ΔT Temperature Difference °C

Chapter 1

Introduction

Thin-film structures have found a wide variety of applications in emerging technologies. For electro-mechanical applications, lead zirconate titanate (PZT) film is commonly used as the actuating or sensing component due to its high piezoelectric constant, high energy density and large electrical-mechanical coupling coefficient. One example of these applications is the piezoelectric micromachined ultrasonic transducer (pMUT) [1-3], where a micromachined multilayered membrane resonator, typically in the order of 10th of micrometers is used as a sound radiating element [1]. Unlike the traditional bulk PZT ceramic based ultrasonic transducers whose operating frequencies are controlled by the dimension of the PZT ceramic, the PZT film in pMUT is mainly used as a component to drive the membranes while the operating frequencies are controlled by the dimensions and properties of the membrane. Thus pMUT offers a more flexible and innovative approach to the development of advanced ultrasonic transducer.

Fabrication of thin film structures is a time-consuming and costly process. As the design flexibility increases, so does the demand for design software which could provide some good insights into the behavior of the structure before it is fabricated. A typical design methodology consists of both analytical study and numerical simulation. The former provides rapid and rational insights, while the latter renders a detailed analysis of the response of the structures. Examples of both approaches as applied to pMUTs can be found in [4] and [5] for the former and the latter respectively. The work presented in this thesis is a follow-up of the study reported in [4]. Before addressing the objectives of the current study, some background information is summarized first.

1.1:Fabrication of pMUT

The thin film membrane structure was made using single side polished, p-type (100) silicon wafers with 76.2mm diameter and 380±20 μm thickness. A flow chart for the overall process is shown in Figure 1. Wafers were first subjected to high temperature wet oxidation at 1050°C in mixed oxygen and nitrogen environment. Oxide layer on polished side of the wafer was then stripped using a buffered oxide etchant (BOE) solution of HF, NH$_4$F, and H$_2$O (10:1) for 10 minutes, while the back-side of the wafer was protected using semiconductor tape. This was followed by boron diffusion on the bare silicon side at 1125°C for 110 minutes to obtain a depth of 2.3μm for boron. Borosilicate glass was removed with a 20 minutes etching in BOE, followed by growing a sacrificial oxide layer by low temperature oxidation (LTO) at 850°C for 2h. The sacrificial LTO layer is then removed in BOE for 10 minutes and final LTO layer is grown. The LTO layer serves as silicon dioxide windows for anisotropic silicon etching. Positive photolithography using AZ5214 as photoresist was carried out to create oxide mask on back-side of the wafer. The exposed silicon was then etched away using ethylenediamine pyrocatechol (EDP) at 110°C for 4.5 hours. This back-side etching resulted in 2μm thick silicon membrane of desired dimensions [5].
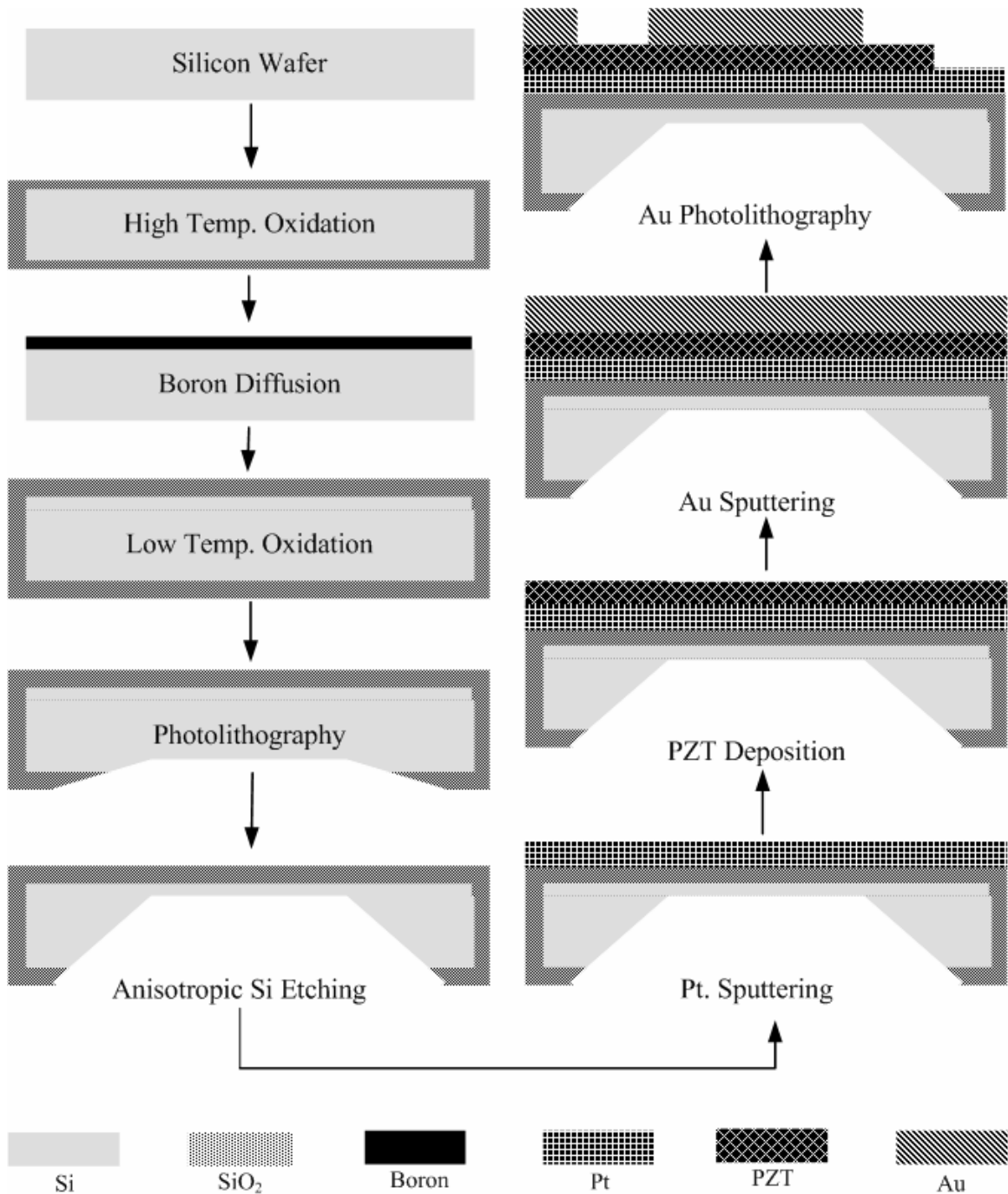
Figure 1 Flow diagram of the fabrication process for pMUT. [5]

After the membrane was fabricated, 5nm of Ti which served as the adhesive layer and 175/200 nm of Pt which served as the bottom electrode layer were DC sputtered on

3

polished side of etched silicon wafer. This was followed by a 10 minute annealing at 650°C. 52/48 PZT was then used as the precursor solution to deposit PZT on the platinized wafer. Afterwards, 5nm of TiW which served as adhesive layer and 200nm of Au layer which served as the top electrode were sputtered. In order to pattern the top electrode, positive photolithography was used. Exposed gold was then etched away using TFA gold etchant (Transene Company, Inc., MA) for 2 minutes and TiW layer was removed using 30% hydrogen peroxide in water for 40 seconds. More details about the fabrication process can also be found in Ref. [6].

A schematic diagram of the side view and pictures of the top view of the fabricated pMUTs are displayed in Figures 2 and 3, respectively. As shown in Figure 3, two different general sizes of pMUTs, small and large (in a relative sense), were designed. The smaller membranes were used to generate higher frequencies. All the designs were created with Corel DRAW software. For the small ones, as shown in Figure 3(a), the widths (W) were varied by 90, 120, 150, and 180μm and the lengths (L) by 860, 1160, 1460, 1760, and 2060μm. The corresponding L/W aspect ratios ranged from 5 to 23. For the large ones, the membranes with the square shape (SM) have the side dimensions of 470, 570, 1070, 1570, and 2070μm respectively, and those with the rectangular shape (RM) have dimensions of 570 μm x 1070 μm, 570 μm x 1570 μm, and 570 μm x 2070 μm, corresponding to L/W aspect ratios of 1.9, 2.8, and 3.6 respectively. The top electrode was slightly smaller than the membrane, i.e. 30μm and 35μm shorter from each side of the membrane for the small and large membranes respectively. For example, for a 180 by 2060μm small membrane, the top electrode size was 120 by 2000μm. The corresponding bottom Pt electrode layer was 175 and 200 nm thick for small and large

membranes, respectively. To apply electric current to the electrode, an electrode pad was placed outside of the membrane and the electrode and electrode pad were connected by connection lead as shown in Figure 3. The sizes of electrode pad and connection lead were 300 by 300μm and 30 by 400μm, respectively.
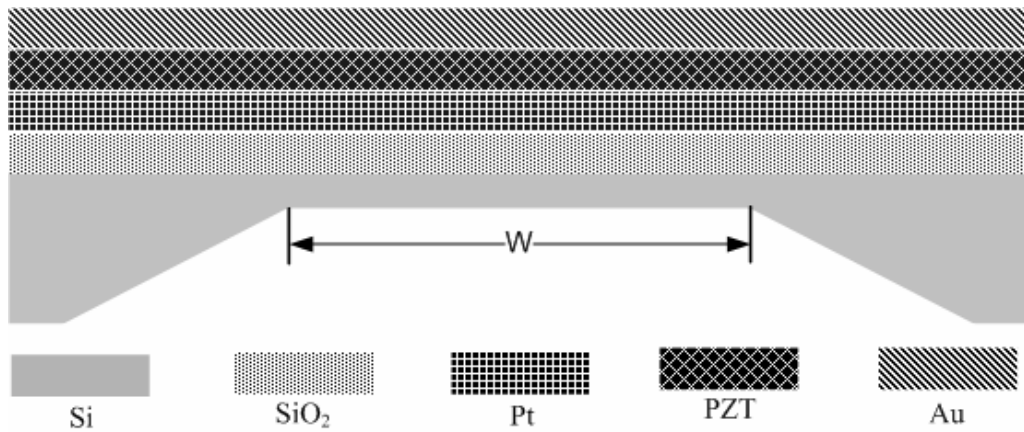
Figure 2 Side view of pMUT membrane structure (not in ratio). [5]

(a)   (b)
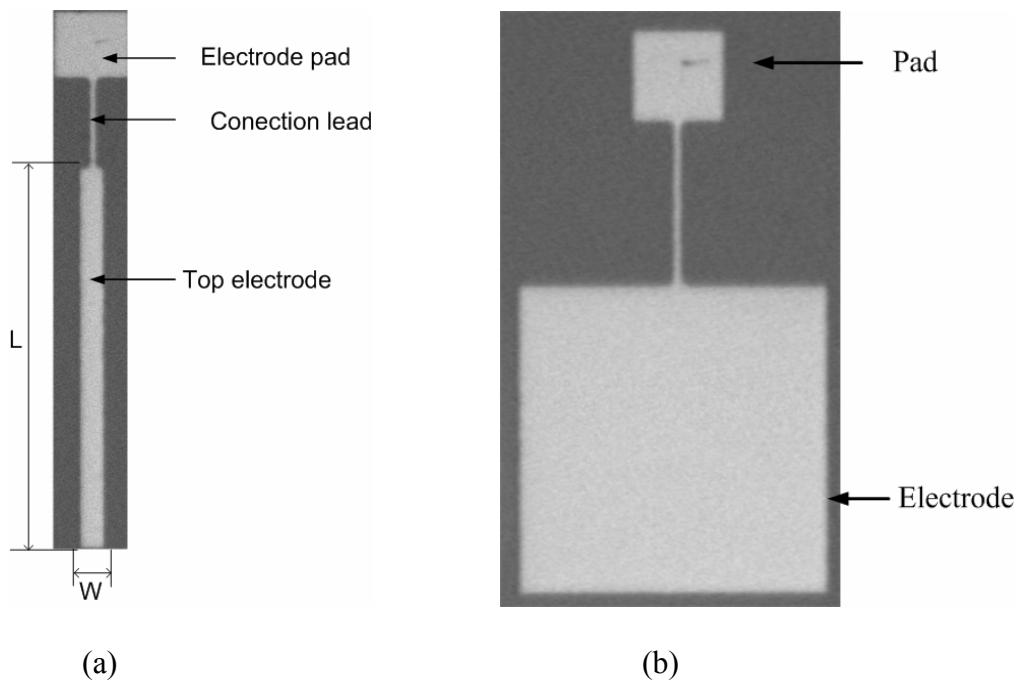
Figure 3 Top view of the pMUT membrane structure. (a) small membrane; (b) large membrane.[5]

1.2: Characterization of pMUT

Characterization of the fabricated pMUTs was done by impedance measurement combined with an equivalent circuit analysis. The impedance was measured with an impedance analyzer and impedance probe kit (Agilent Technologies, 4294A Precision Impedance Analyzer, 42941A Impedance Probe Kit). The sample was elevated in the air by 1cm from the surface of the probe station and the measurement was done in air. A typical impedance measurement result is shown in Figure4a. The resonance frequency (f_s) and anti-resonance frequency (f_p) are directly displayed from these measurements. These two values are very close to each other and can be approximated as the mechanical resonance frequency of pMUTs. The resonance frequencies for the aforementioned pMUTs are shown in Figure 4b as symbols. Once f_s and f_p are known, the effective coupling coefficient $\left(k_{eff}^2 \right)$ can be determined as

$$k_{eff}^2 = \frac{f_p^2 - f_s^2}{f_p^2}$$

1.1
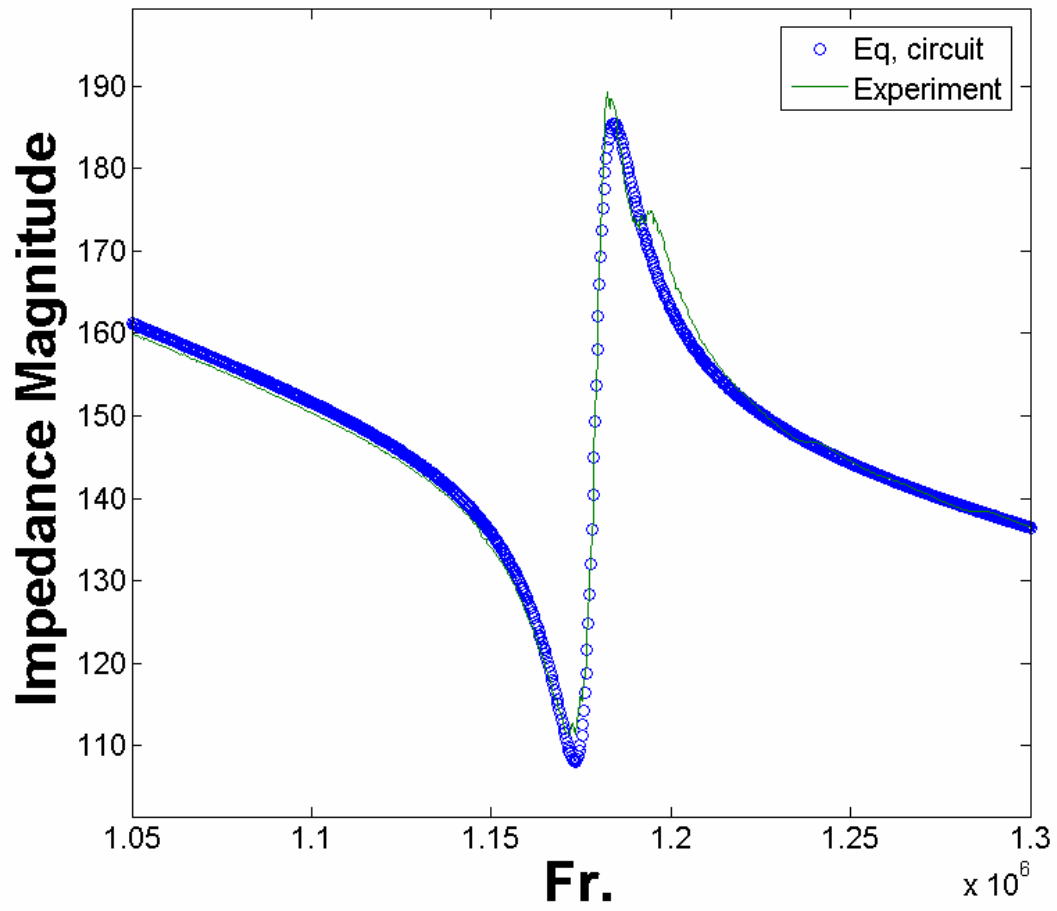
(a)
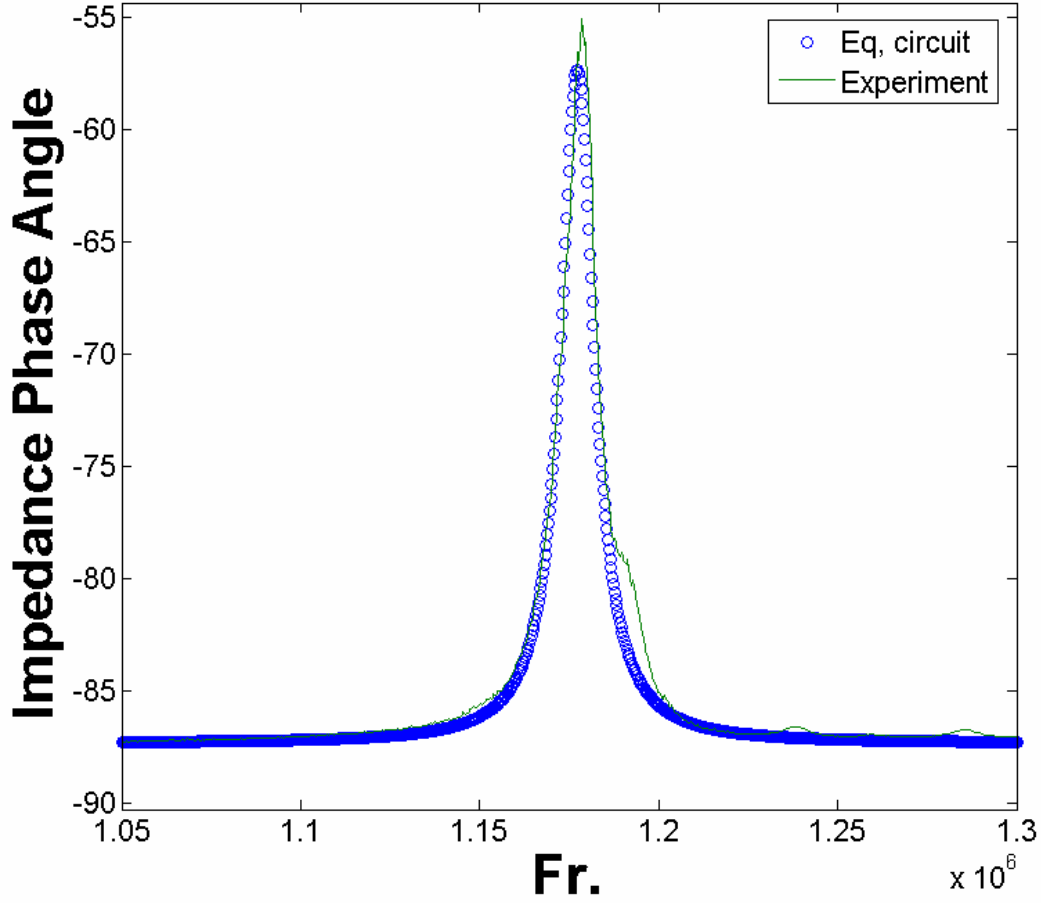
(b)

Figure 4: (a) Impedance magnitude; (b) Impedance phase angle. Solid lines represent the experimental data and symbols represent the curve-fitted results based on equivalent circuit.[7]

1.3: Finite element analysis based on a combination of the equivalent single-layer theory and the classical laminated plate theory (CLPT)

In [5], a finite element analysis was used to predict the resonance frequencies of the aforementioned pMUTs. The formulation was based on the equivalent single-layer theory and the classical laminated plate theory (CLPT) developed by Reddy [8, 9]. In the equivalent single-layer theory, the multi-layered composite is transformed into an

8

equivalent single layer. The CLPT was based on the classical Kirchhoff hypothesis for thin plate such as the transverse normal to midsurface of the plate remains straight and normal to the midsurface before and after the deformation, and the plate is inextensible in the normal direction. For composite plates, it is further assumed that the layers are perfectly bonded together, i.e. there is no delamination between the layers. A comparison of the predictions based on the developed code and experimental data is shown in Figure 5.
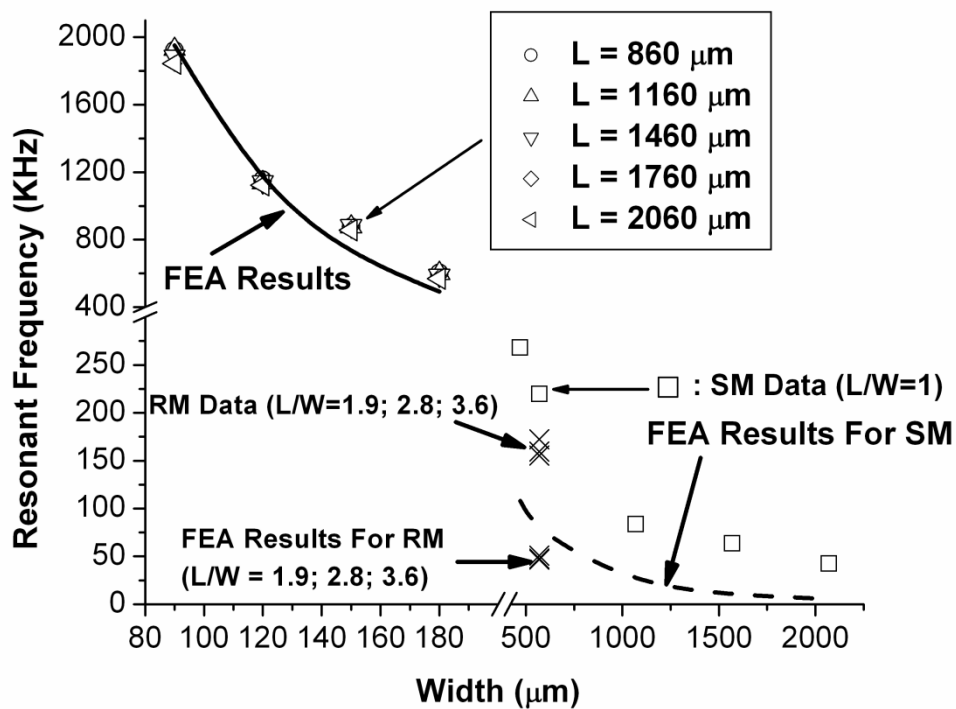
Figure 5: Experimental data (symbols) and FEA results (solid and dashed lines) for the thin film membrane structures. [5]

As shown in Figure 5, the calculations matched fairly well with the data for the small membranes. However, they underestimated the frequencies for large membranes, both SM and RM. The calculations also showed some length dependence for large membranes, but little for small ones.

One most probable reason for the quantitative discrepancies observed in Figure 5 is the residual stress. The residual stress is likely to be generated during the micro fabrication process due to the different thermal expansion coefficients for different layer materials. As mentioned earlier, platinum layer was annealed at 650^oC for 10 minutes after DC sputtering to avoid delamination between SiO_2 and platinum layers. After annealing, the wafer was cooled at a rate of $100°C/min$ to room temperature [9]. This thermal cycling process would undoubtedly generate some residual stress in the structure. One of the significant consequences from the residual stress is the shape distortion. In the aforementioned calculations, the membranes were all assumed to be flat. A distorted membrane, e.g. a dome-shaped membrane, would certainly have different dynamic responses than flat membranes. Between small and large membranes, the shape of the latter would be expected to be affected more by residual stress due to its larger flexibility.

Besides the residual stress, the difficulty in obtaining the precise measurement of the dimensions and material properties of the thin film structures could also contribute to the discrepancies. Furthermore, it has been observed by Choi et al [5], Baborowski et al. [10] and Muralt et al. [11] that the fundamental frequencies increase with the increase of DC bias voltage. The parasitic capacitance by the square pad and connection leads were also observed to have some effects on the dynamic behavior of the thin membrane structures.

Finally, it should also be mentioned that the boundary condition used in the [5] was clamped condition which implied infinite rotational stiffness for the support. For the pMUTs fabricated in this study, the size of the membrane portion was very small compared to that of the support which constituted the rest of the structure. Thus clamped boundary condition seemed to be reasonable and was not expected to be a contributor to the discrepancies observed here. However for a more general membrane structure with a shape similar to that illustrated in Figure 2, the actual boundary conditions for the membrane could be quite complicated. The size, geometry, and material properties for the support could all affect the stiffness of the support relative to that the membrane.

Chapter 2

Objectives and Approach

The overall objective of the current research is to gain some insights into the discrepancies between the calculations and experimental data of ultrasonic transducers observed in Figure 5 [5]. The focus is on the effects of geometric variation and the residual stress on the resonance frequencies of the thin membrane structures. Furthermore, since the membranes with the sizes that are greater than 500 μm have the most profound discrepancies, special attention is paid to these types of membranes.

The approach used in this study is again by numerical simulation. The effects of geometric variation are investigated first. Because the residual stress would result in distorted membrane shape, the effects of shape variation are studied next. Finally, the fabrication process is simulated as a cyclic thermal-mechanical process, and the resultant residual stress is estimated and the corresponding distorted shape is determined. The distorted shape is then used as the input for the dynamic analysis.

The software used in this study is ANSYS 10.0. The reasons for using ANSYS instead of the FORTRAN code developed in [5] are the following. Firstly, ANSYS can be used as another verification tool for the developed code. Secondly, ANSYS has the capability to study the dynamic responses of curved structures. Thirdly, ANSYS has the capability for simulating the thermal-mechanical cycling process. Finally, ANSYS is code that has well established pre and post processing capabilities.

Chapter 3

ANSYS Analysis

ANSYS is a self contained analysis tool incorporating pre-processing (geometry creation, meshing), solver and post processing modules in a unified graphical user interface. It is a general purpose finite element modeling package for numerically solving a wide variety of engineering problems, including static/dynamic structural analysis (both linear and non-linear), heat transfer and fluid problems, as well as acoustic and electromagnetic problems. A brief introduction of the code is given in the following sections.

3.1: General Procedure for ANSYS Finite Element Analysis

A typical analysis consists of several main steps:

a.   Building the Model

b.   Applying Loads and Obtaining the Solution

c.   Reviewing the Results

3.1.1 Building the Model:

First, a jobname and analysis title needs to be specified in the beginning of the progress. By using a jobname for each analysis, user can ensure that no files are overwritten. Next, the element types, material properties, the model geometry, and creation of the meshes are specified and accomplished within the preprocessing part of

the code, namely, PREP7. ANSYS contains more than 150 different element types in its element library. Each element type has a unique number and a prefix that identifies the element category [12]. User can select a suitable element type from this library (Figure6). In this study, elements SHELL99, SOILD191, SOLID45, and PLAN42 were used for this study. Elements SHELL99 and SOLID191 were used for dynamic modal analysis and PLANE42 and SOLID45 were used for 2-D and 3-D thermal loading static analysis, respectively. SHELL99 and SOLID191are considered as 2D models.
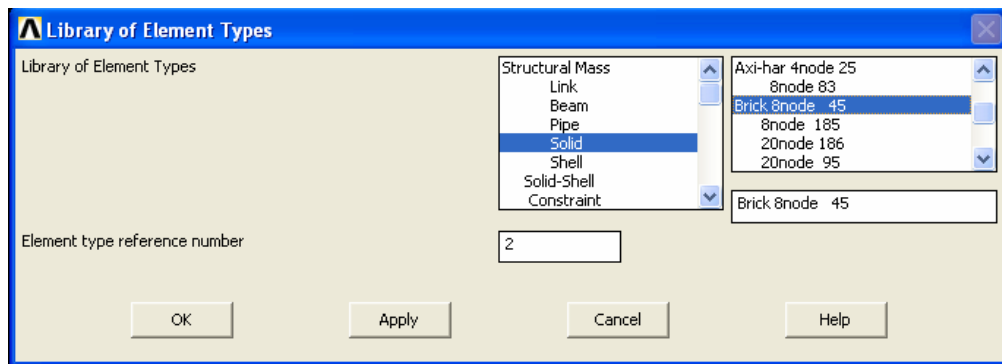
Figure 6: Dialog box for element type selecting

Model Creation:

Keypoints: When the solid model generation approach is used, user can start by generating keypoints. The keypoints are necessary to create higher-order entity for different modeling geometries such as lines, areas, and volumes. In the keypoints creation, ANSYS brings a dialog box and asks for four fields for the keypoint number, and the x-, y-, and z-coordinates. Once the needed information is provided, the keypoints will be displayed on the WorkingPlane.

14

Lines: Lines are used to create a mesh with line element or creating areas and volumes. A straight and cubic spline can be created. A straight line is created by connecting any two keypoints (Figure7). For the cubic spline line, ANSYS requires several keypopints (minimum 2) and generate a spline by picked points (Figure8)
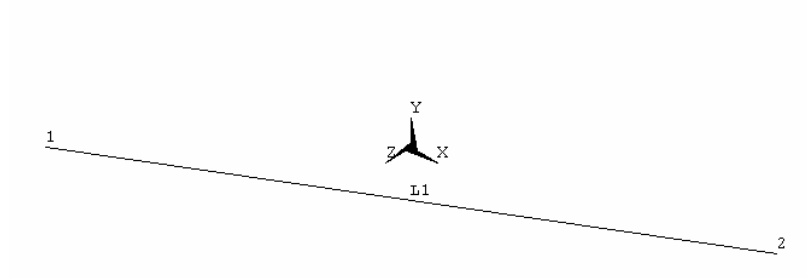
Figure 7: A straight line
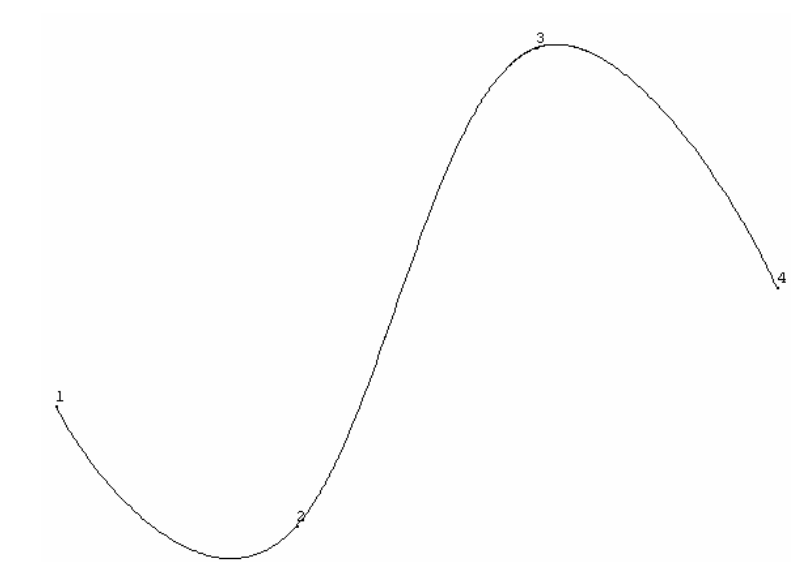
Figure 8: A cubic spline line

Areas: Areas are used to create a mesh with area elements and to create volumes. When creating areas by lines, ANSYS requires minimum of 3 lines and maximum of 10 lines and they must be co-planer. All lines have to be picked either in clockwise or counterclockwise order.

Volume: Volume is used to create a mesh with volume element. Volume can be created by keypoints or areas. If keypoints are used, the lines and areas associate with the volume will be generated automatically. If areas are used, ANSYS requires at least four continually areas to form a volume

Defining Material Properties:

After an element type has been selected, user can input linear or non-linear material properties in the selection window (Figure9) as required by the selected material model. Each set of material properties has a material reference number (Figure10). The table of material reference numbers versus material property sets is called the *material table*. Within one analysis, user may have multiple material properties, and ANSYS identifies each set with a unique reference number [12].

As mentioned earlier, SHELL99 and SOLID191 are 2-D meshing geometries. The mutiple material properties entered for each layer are used to determine the material properties for the equivalent layer. In addition to material properties, layer material angles and layer thickness also need to be entered (Figure11).

16
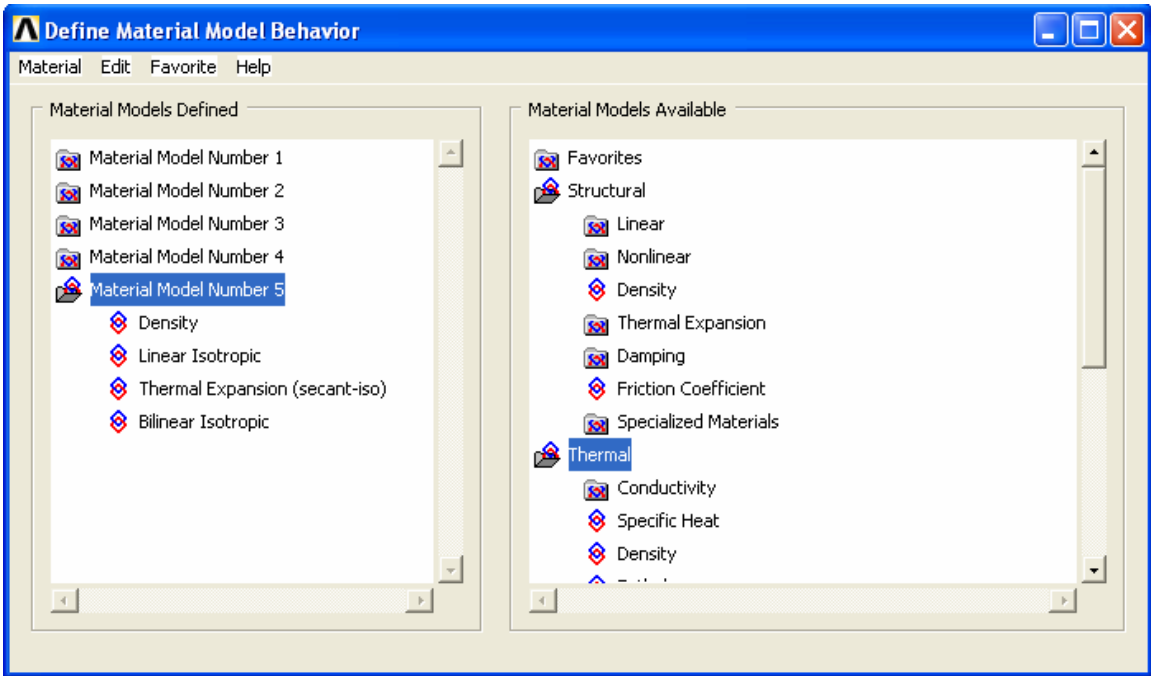
Figure 9: Dialog box for material properties input selecting list
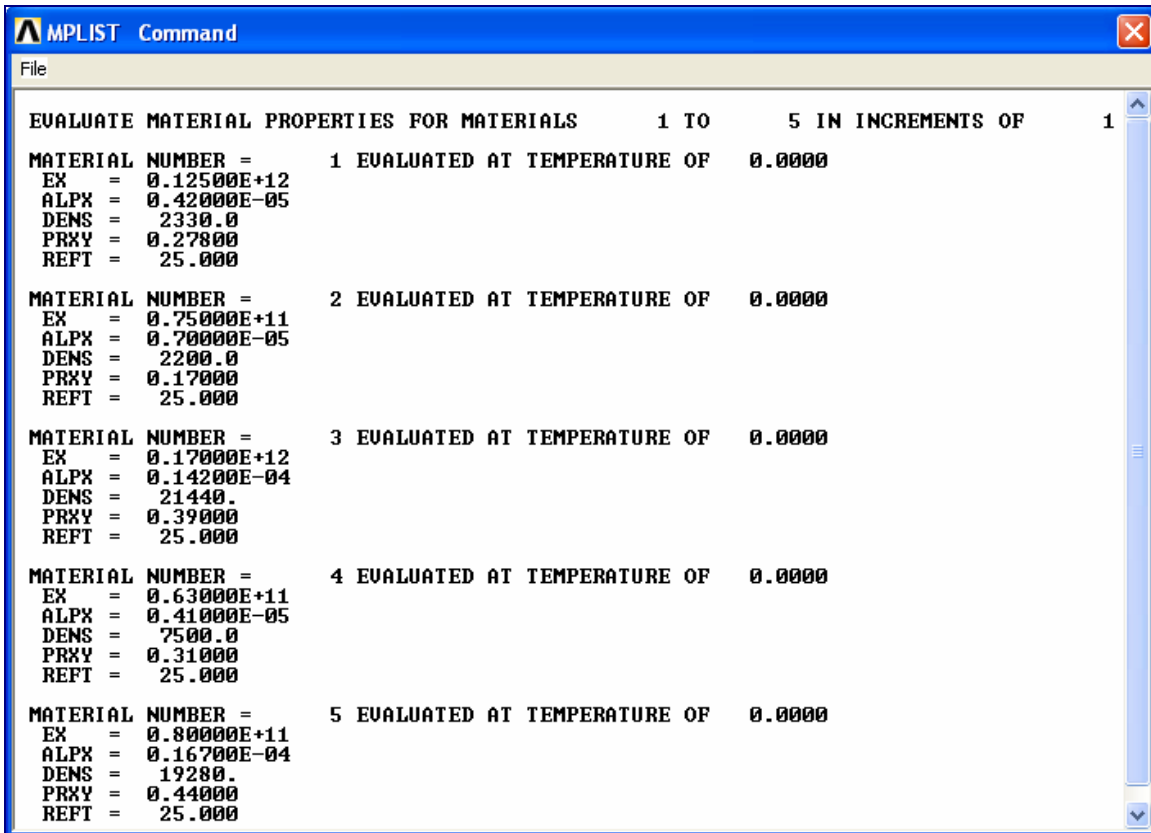
Figure 10: List of material properties input
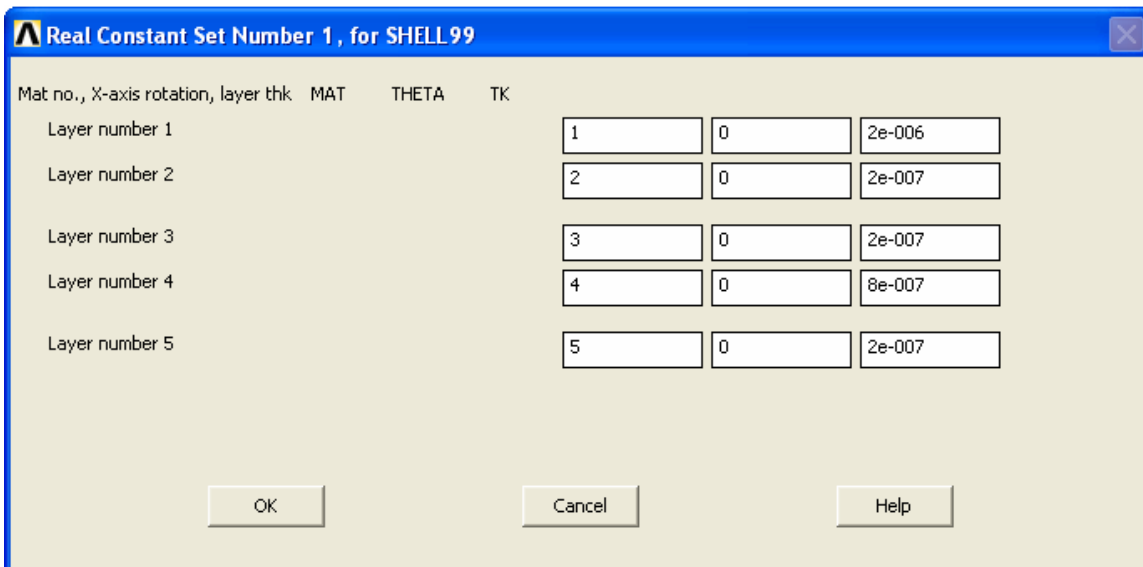
Figure 11: Dialog box for layers thickness input

Creating the Finite Element Mesh:

Once the solid model is built; element attributes are established; material properties are entered; and meshing controls are set, ANSYS is then ready to generate the finite element model. ANSYS has two ways to generate the finite element model, namely, solid modeling and direct generation. For the method of *solid modeling*, user can describe the geometric shape (triangular or rectangular) and size control for the element, and then instruct the ANSYS program to automatically *mesh* the geometry with nodes and elements. The method of *direct generation*, user can "manually" defines the location of each node and the connectivity of each element. Several convenient operations, such as copying patterns of existing nodes and elements, symmetry reflection, etc. are available [12]. In this study, *solid modeling* method was used to create finite element model. The size control for the element was accomplished by specifying the element edge length or number of element divisions (Figure12). The model will then be meshed automatically with the selected element (Figure13).
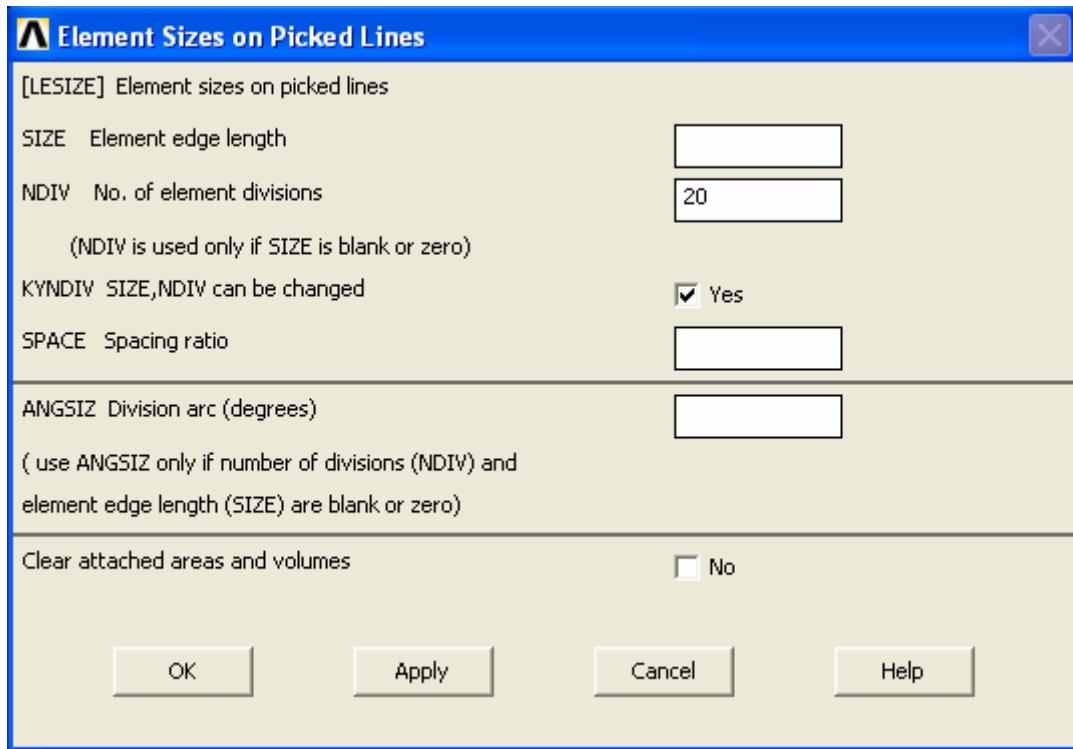
Figure 12: Dialog box for meshing size control window
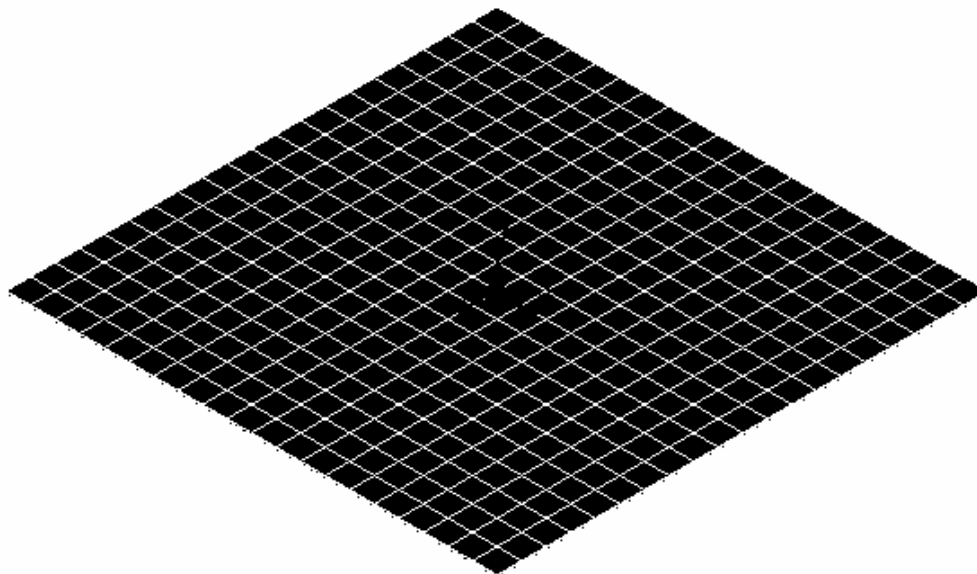
Figure 13: Sample finite element model

3.1.2 Applying Loads and Obtaining the Solution:

Defining the Analysis Type and Analysis Options:

The analysis options used in the current study are structural and thermal analysis. In structural analysis, user can choose different types of analysis method based on the loading conditions and the types of response to be studied. For example, if the problem is the applied load and support conditions of the solid body do not change with time, user would choice a static analysis. If the analysis concerns natural frequency and mode shapes of a structure, user would choose a modal analysis. For time-dependent problems, there are two analysis methods: harmonic analysis and transient dynamic. Transient dynamic allows obtaining the response of a structure subjected to loads with arbitrary behavior in time, but harmonic analysis only allows exhibiting sinusoidal in time. In this study, static analysis and modal analysis are used for thermal loading simulation and fundamental frequency analysis, respectively. In the modal analysis, The code solves the eigenvalues and eigenvectors of the governing dynamic equations. The eigenvalues and eigenvectors correspond to the natural frequencies and the corresponding mode shapes respectively.

In the thermal analysis, ANSYS solves steady-state or transient heat transfer problems including conduction, convection, radiation problems and phase changes associated with melting or freezing. One special case is the so-called thermomechanical analysis in which the displacement, stress, and strain fields due to different thermal expansion coefficients are calculated.

Applying Boundary Conditions:

For a well-defined mathematical problem, the condition along the entire boundary must be known. These conditions are referred to as the *boundary conditions*. In the structure analysis problems, the primary variables are the displacement components. When the primary variables are used, the prescribed displacement will be specified along on the boundary. The other type of boundary condition is the traction which is a secondary variable and is related to the derivative of the primary variables. In the thermal analysis problems, the primary variables are the temperature and the associated secondary variables are the corresponding heat fluxes.

The boundary conditions can be applied at the nodes, lines, areas, or volumes. For the latter, the prescribe loads are converted to equivalent nodal loads during the calculation.

Solving the Problem:

After completing the construction and meshing the model, determining the type of analysis, and specifying the loading conditions (boundary, initial, and body loads), the problem can be solved.

3.1.3 Reviewing the Results:

After the solution has been obtained, the results are read into the database and the user can review results through graphics displays. The types of graphics displays available are deformed shapes (structure analysis), contour plots, vector displays, and path plots.

In the structure analyses, three options are available to the uses for displaying the deformed shape: display deformed shape only, display deformed and unreformed shapes together, and display deformed shape with the outer boundary of the unreformed shape, through the *Plot Deformed Shape* dialog box (Figure 14). After user makes a choice , the deformed shape and modal shapes can be displayed in the *Graphics Window* (Figure15). In addition, ANSYS also allows user to review the distribution of different types of stresses or temperatures in the structure.
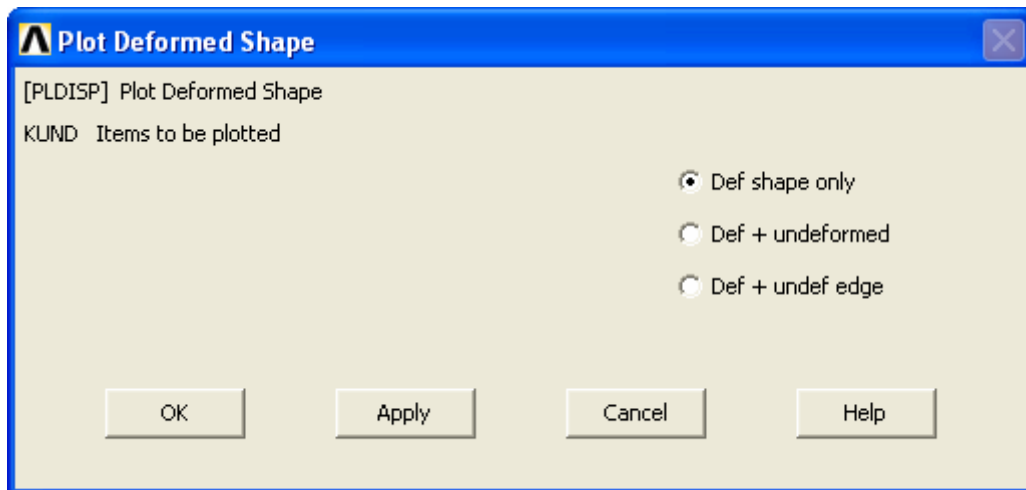
Figure 14: Dialog box of Plot Deformed Shape options.
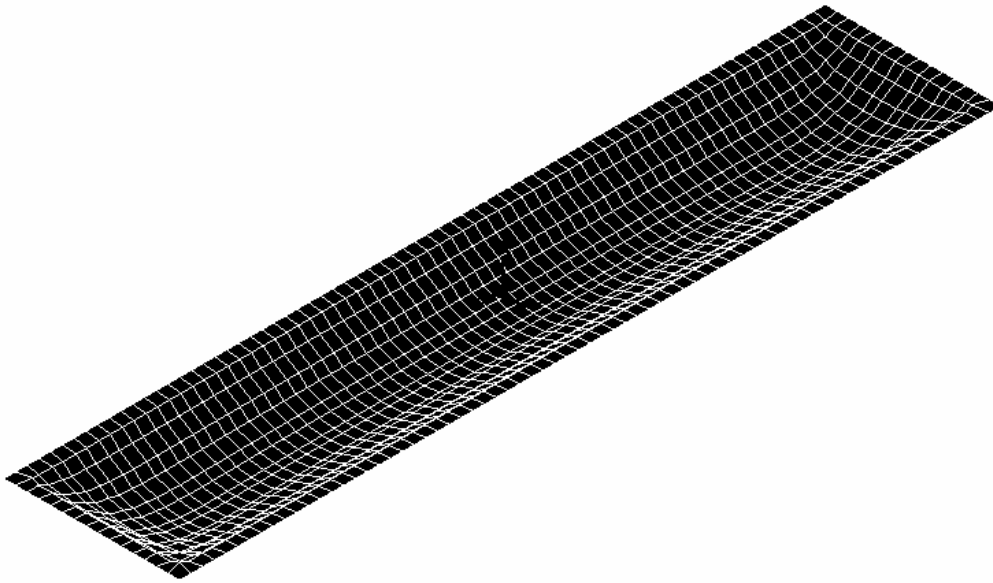
Figure 15: Deformed shape appears in graphics window.

In addition, ANSYS also allows users to obtain line plots along a defined path. Users can define various paths by user-defined specifications and number of divisions between data points. Once the paths are defined, the physical quantities along the path can be plotted in the *Graphic Window*.

3.2: Attributes of the element used and material properties

As mentioned earlier, four types of elements, SHELL99, PLANE42, SOLID45, and SOLID191, were used in this study. Their detailed attributes are discussed in

following section. In addition, the relevant material properties used in this study are also presented at the end of the section.

3.2.1 SHELL99

SHELL99 may be used for analyzing layered shell structures. The geometry, node locations, and the coordinate system for this element are shown in Figure16. The element has eight nodes; I, J, K, L, M, N, O, and P and each node has six degrees of freedom: translations in the nodal x, y, and z directions and rotations about the nodal x, y, and z-axes. The element allows up to 250 layers with different layer material direction angles and orthotropic material properties. Surface loads can be applied to face 1 (I-J-K-L) (bottom, in +Z direction), face 2 (I-J-K-L) (top, in -Z direction), face3 (J-I), face 4 (K-J), face 5 (L-K), and face 6 (I-L). Input temperatures T(I), T(J), T(K),T(L), T(M), T(N), T(O), and T(P) can be specified at nodes I to P, respectively. A triangular-shaped element may be formed by defining the same node number for nodes K, L and O. The output data include nodal displacements and element stress with respect to the layer local coordinate directions [12].
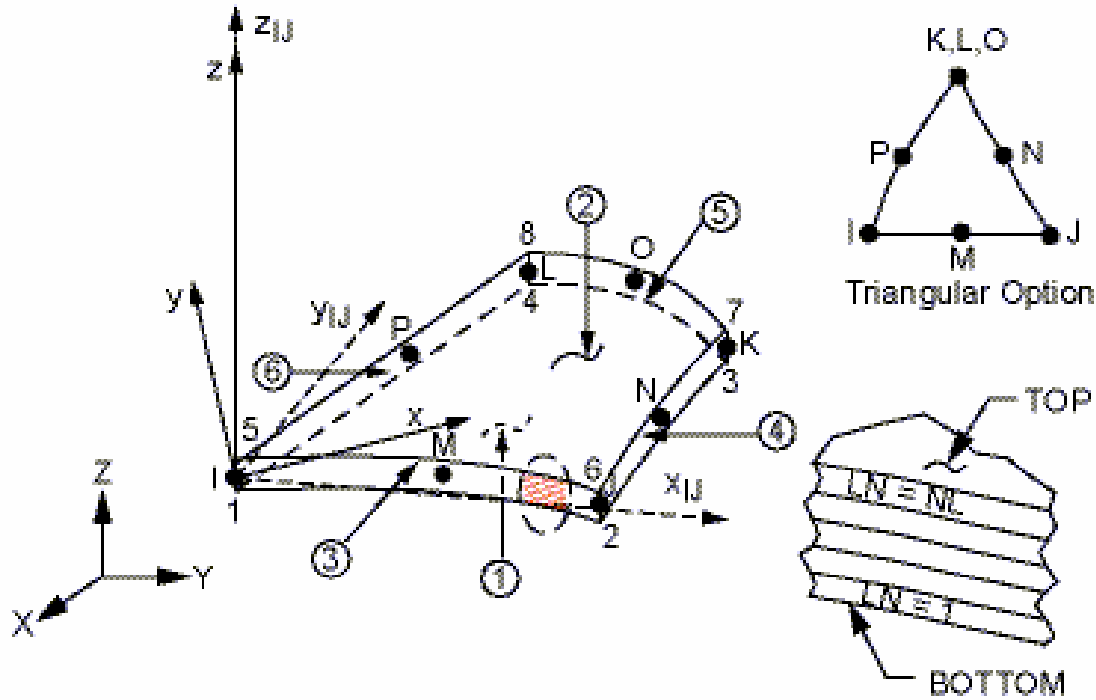
Figure 16: SHELL99 geometry [12]

3.2.2 PLANE42

PLANE42 may be used for 2-D modeling of solid structures. The element can be used either as a plane element (plane stress or plane strain) or as an axisymmetric element. The geometry, node locations, and the coordinate system for this element are shown in Figure17. The element is defined by four nodes, I, J, K, and L. Each node has two degrees of freedom: translations in the x and y directions. The element has plasticity, creep, swelling, stress stiffening, large deflection, and large strain capabilities. The element also allows inputting orthotropic material directions with respect to the element coordinate directions. Pressures may be input as surface loads on the element faces as shown by the circled numbers. Temperatures, T(I), T(J), T(K), and T(L) may be input as element body loads at the nodes I, J, K, and L, respectively. Element PLANE42 carries

out nodal displacements included in the overall nodal solution and element stress. The element stress directions are parallel to the element coordinate system and correspond to the layer local coordinate directions [12].
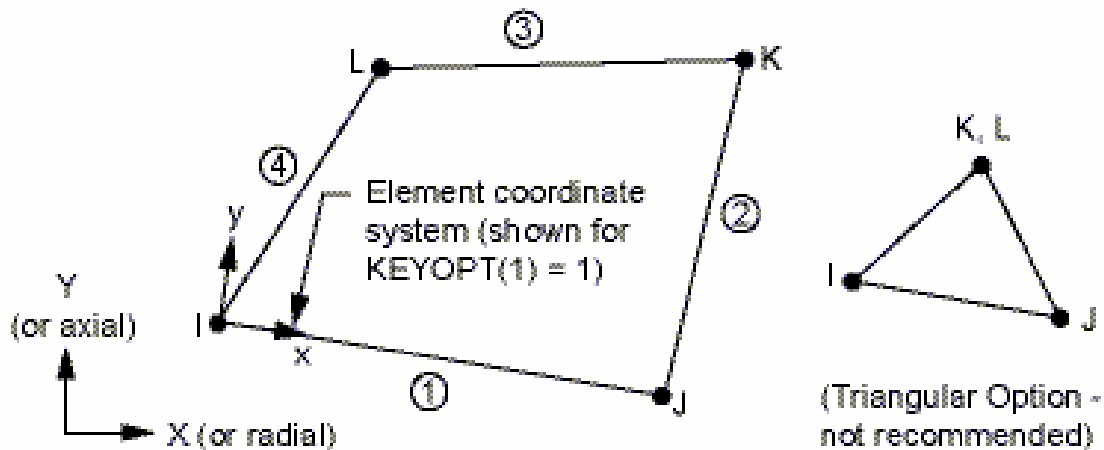
Figure 17: PLAN42 geometry [12]

3.2.3 SOLID45

SOLID45 may be used for the 3-D modeling of solid structures. The geometry, node locations, and the coordinate system for this element are shown in Figure18. The element SOLID45 is defined by eight nodes; I, J, K, L, M, N, O, and P. Each node has three degrees of freedom: translations in the nodal x, y, and z directions. The element has plasticity, creep, swelling, stress stiffening, large deflection, and large strain capabilities. A reduced integration option with hourglass control is available. The element allows inputting orthotropic material directions with respect to the element coordinate directions.

27

Temperatures, T(I), T(J), T(K), T(L), T(M), T(N), T(O), and T(P) may be input as

element body loads at the nodes I to P, respectively. The output data include nodal

displacements included in the overall nodal solution, element stress directions with

respect to the element coordinate system, and surface stress with respect to the surface

coordinate systems [12].
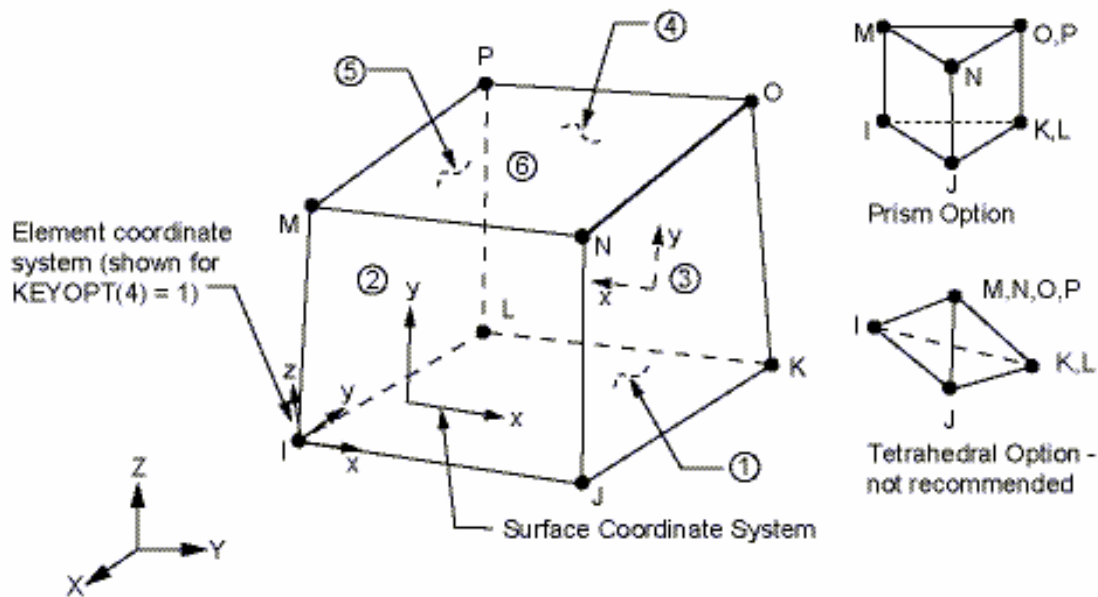
Figure 18: SOLID45 geometry [12]

3.2.4 SOLID191

SOLID191 is a layered version of the 20-node structural solid and a higher order

version of the 3-D 8-node solid element SOLID45 and is designed to model layered thick

shells or solids. The geometry, node locations, and the coordinate system for this element

are shown in Figure 19. The element SOLID191 has 20 nodes, I, J, K,…, W, X, Y, Z, A,

28

and B, and each node has three degrees of freedom: translations in the nodal x, y, and z

directions. The element allows up to 100 different material layers, layer thicknesses, and

layer material direction angles and orthotropic material properties. The surface loads can

be applied to face 1 (J-I-L-K), face 2 (I-J-N-M), face 3 (J-K-O-N), face 4 (K-L-P-O), face

5 (L-I-M-P), and face 6 (M-N-O-P). Body loads are allowed to input temperature T1, T2,

T3, T4 at bottom of layer 1, T5, T6, T7, T8 between layers 1-2, similarly for between

next layers, ending with temperatures at top of layer $NL(4*(NL+1)$ maximum). The

output data include nodal displacements in the overall nodal and the element stress

directions correspond to the layer local coordinate directions [12].
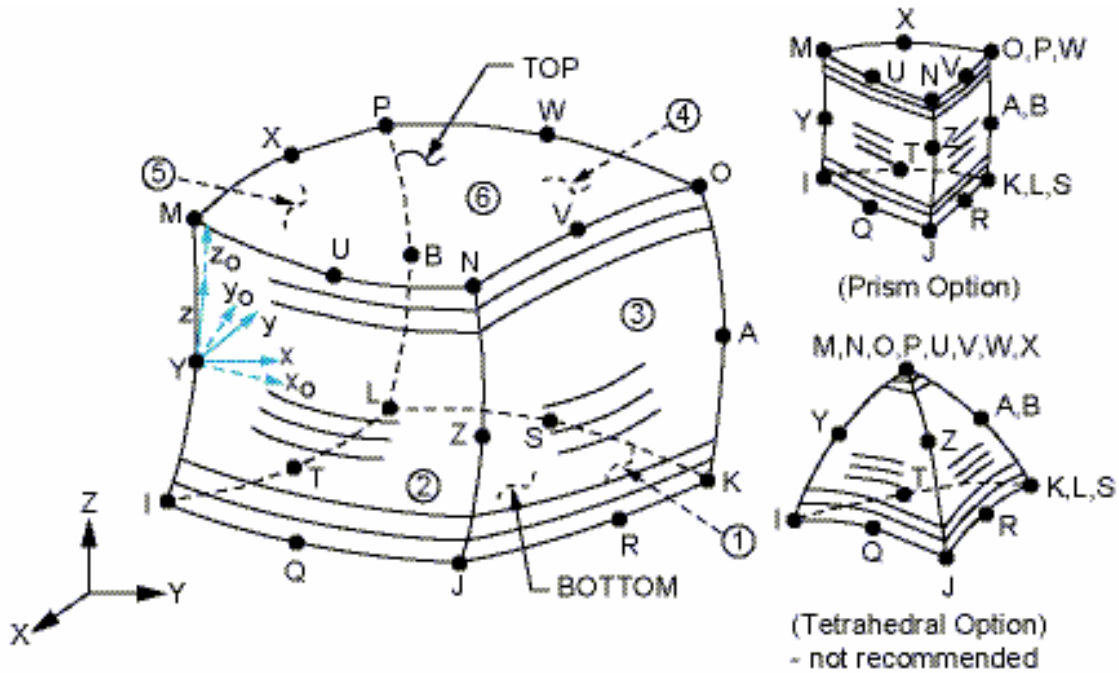
Figure 19: SOLID191 geometry [12]

3.3: Material properties

The material properties and nominal layer thicknesses used in the analysis follow those used in [5] and are listed in Table 1.

Table 1. Material properties and nominal layer thicknesses used in the analysis.

	E(Gpa)	ν	ρ (Kg/M^3)	$\sigma_{(yp)}$(MPa)	α (10^{-6}/K^0)	Thickness(μ m)
Si	125	0.278	2330	501[13.]	4.2 [18.]	2.0
SiO$_2$	75	0.17	2200	200[14.]	7.0 [19.]	0.2
Pt	170	0.39	21440	30[15.]	8.9 [20.]	0.2
PZT	63	0.31	7500	600[16.]	4.1 [18.]	0.8
Gold	80	0.44	19280	55[17.]	15.18[21.]	0.2

Chapter 4

Effect of dimensional variation on the resonance frequency

During the fabrication process, an operator typically follows the fabrication recipe to manufacture the thin membrane structures. Several factors such as temperature, timing, pressure, and air flow rates could all affect the final thickness of each layer for the fabricated structures. Furthermore, for the measurement of in-plane dimensions, the operator typically measures them on the token pictures. The edges of the structures are typically not perfectly etched and the operator has to pick up reasonable starting and ending points for the measurement of in-plane dimensions. All the above factors could contribute to the uncertainty of the final dimensions of the structure. According to Choi el al [5], the uncertainty is typically $\pm 15\%$. In this part of the study, the effects of this $\pm 15\%$ uncertainty for the structure dimensions on the resonance frequencies are investigated.

4.1: Comparison of the results from ANSYS and the developed code

Before the effects of dimensional variation were investigated in this study, ANSYS was first used to repeat the calculations reported in [5], and the results were compared with those reported in [5]. Two types of elements were also tested, namely, SHELL99 and SOLID191. The geometry, node locations, and the coordinate system for these elements were described in section 3.2.1 and 3.2.3, respectively. Two groups of structures, rectangular and square, in micron scale were investigated. The former has

sizes of 90 by 860, 120 by 860, 150 by 860, and 180 by 860 and the latter has 570, 1070,

1570, and 2070. The boundary conditions used are clamped condition. The structures

were considered to be flat and were meshed in quadrilateral shape. The comparisons of

finite element analysis (ANSYS and FEA code) with experimental results for the above

structures are shown in Figure20 and Figure21, respectively.

As shown in Figures 20 and 21, both results matched with each other quite well.

The differences are less than 3%. These results not only provided a further verification of

the results reported in [5], but also establish a baseline for using ANSYS for further

investigation. As also indicated by these figures, the results based on SHELL99 and

SOLID191 were also very close to each other. However, SHELL99 was chosen as the

element for the subsequent analysis based on the following reasons. Firstly, the

SHELL99 needs less computing time than SOLID191. This is because SOLID191 has

twelve more nodes than SHELL99. In the finite element analysis, the sizes of the stiffness

$[K]$ and mass $[M]$ matrix and the corresponding computing time are increased by the

increasing nodes. Secondly, SHELL99 has six degree of freedoms which includes

translations in the nodal x, y, and z directions and rotations about the nodal x, y, and z-

axes, but SOLID191 only has translations in the nodal x, y, and z direction. The rotation

degree of freedom will give more flexibility in the structure and give more accurate

results in resultant frequencies.

For the rectangular structures, the resultant frequencies from experimental, FEA

calculations and ANSYS simulations all follow the same trend as shown in Figure 20.

Frequencies for the membranes with the sizes of 90 by 860 and 120 by 860 are 1.5% and

7% lower than experimental results, respectively, and are within the 15% range of

variation for the experiment data. For both rectangular and square membranes, the difference between experimental data and finite element analysis (ANSYS and FEA code) increased with the increase of dimension. Generally speaking, the frequencies of rectangular membranes whose widths were less than 200μm match fairly well to fabrication chips data, but the square membranes whose widths were greater than 500μm have 65% to 86% difference compared to the experimental data. Accordingly, the subsequent studies are focused on the square membranes.
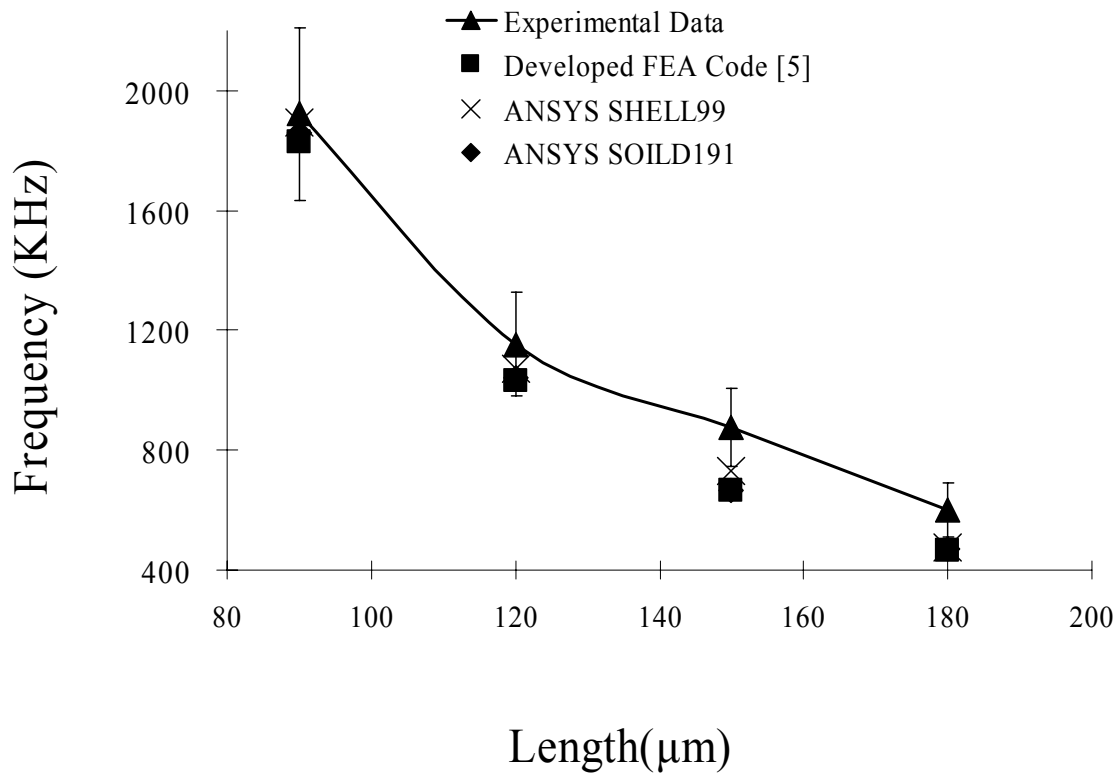
Figure 20: ANSYS rectangular flat plate results compare to experimental data and FEA results for the thin film membrane structures with width less than 500 μm.
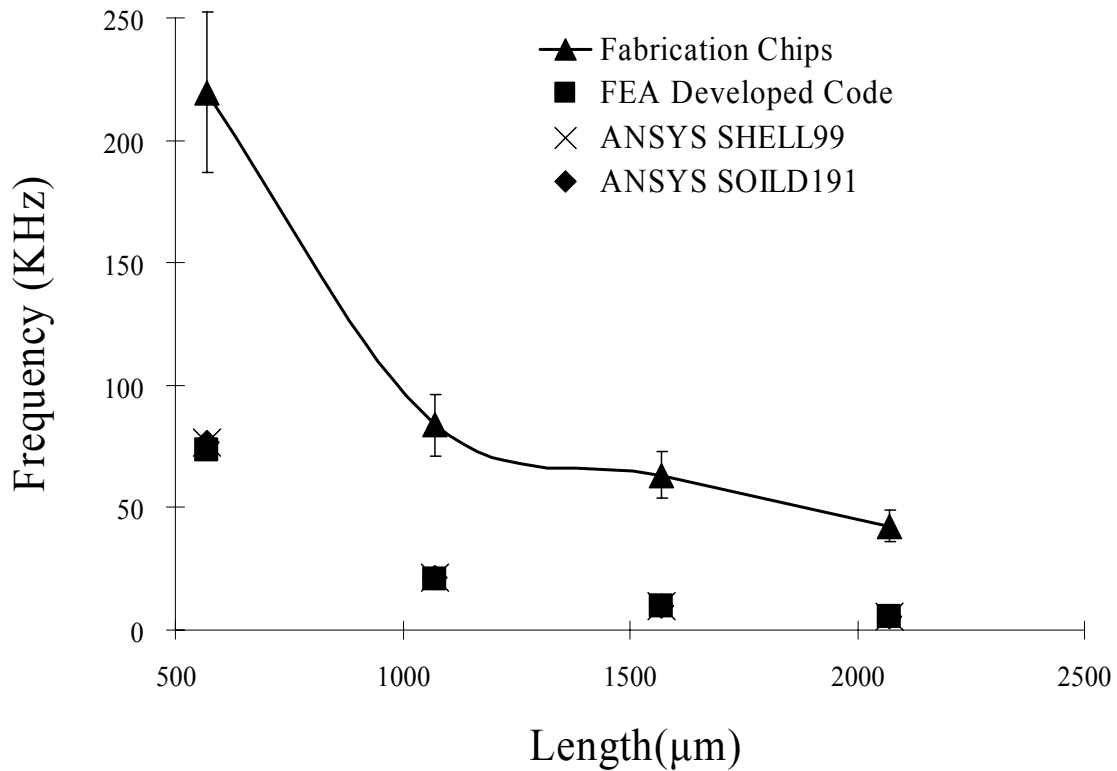
Figure 21: ANSYS square flat plate results compare to experimental data and FEA results for the thin film membrane structures with width greater than500 μm. (change "Fabrication Chips" to "Experimental Data")

4.3: Effect of variation of thickness

For the thickness uncertainty analysis, Choi el al [5] has demonstrated that the fundamental frequencies increased with the thickness of the layers. As mentioned earlier, the uncertainty range for the thickness is about 15%. In this part of the study, the thickness was varied in different ways to examine its effects on resonance frequencies. The membrane examined has a size of 570 by 570 μm . In the first case, an increase of thickness of 0.51μm is applied to each layer. In the second case, a 15% increase of thickness is applied to each layer. In the third case, different amount of thickness increases were applied to different layers. The results are summarized in Table 2.

Material properties play a critical role on the frequency of the structure. The fundamental frequency ω can be defined as [22]

$$\omega = \sqrt{\frac{K}{M}} \qquad\qquad 4.1$$

where K is presenting the stiffness matrix and M is presenting the mass matrix. In the finite element analysis, the increased layer thickness will enlarge the material stiffness matrix $[K]$ and mass matrix $[M]$. The magnitude of stiffness matrix $[K]$ will have more increment than mass matrix $[M]$ because the magnitude of Young's modulus is way greater than that of density. Therefore, the increased layer thickness will result greater fundamental frequency according to equation 4.1. From Table1, we can see that silicon has largest Young's modulus and least density compared to other materials. Thus change of silicon layer thickness results in the largest increments in frequency. Silicon dioxide has the second largest ratio between Young's modulus and density. Thus it also has significant influence on the resultant frequency. Gold and platinum has less relative ratios between Young's modulus and density. Consequently their influence is smaller. However, none of the above thickness variations can increase the frequency to experimentally measured one, i.e. 219 KHz.

Table 2.ANSYS frequency results effect of thickness variation

Lyaer thickness(μm)→ Membrane size(μm) ↓	Si	SiO$_2$	Pt	PZT	Au	Total Thickness	Frequency (KHz)
570 by 570	2	0.2	0.2	0.8	0.2	3.4	75.2
570 by570	2.51	0.2	0.2	0.8	0.2	3.9	90.6
570 by570	2	0.71	0.2	0.8	0.2	3.9	90.1
570 by570	2	0.2	0.71	0.8	0.2	3.9	76.0
570 by570	2	0.2	0.2	1.31	0.2	3.9	85.9
570 by570	2	0.2	0.2	0.8	0.71	3.9	76.8
570 by570	2.3	0.23	0.23	0.92	0.23	3.9	86.4
570 by570	2.4	0.3	0.23	1.1	0.23	4.26	93.9

* Experimental frequency measurement for 570 μm square membrane is 219 KHz

4.4: Effect of variation of the in-plane dimensions

As mentioned earlier, the measurement of in-plane dimensions were based on the token picture. The operator has to define the starting and ending points on the uneven surface somewhat arbitrarily. This would result in some uncertainty in the in-plane dimension measurement. In this part of the study, the effect of ±15% uncertainty for the in-plane dimensions was investigated for the same 570 by 570 μm square membrane. The results are summarized in Table 3, which shows that the resultant frequency increases with the decrease of in-plane dimensions.

Table 3. ANSYS frequency results effect of in-plane dimension variation

Membrane size(μm) ↓	error(%)	Frequency(KHz)
485 by 485	-15%	103.8
513 by 513	-10%	92.8
541 by 541	-5%	83.4
570 by 570	0%	75.2
598 by 598	5%	68.3
627 by 627	10%	62.1
655 by 655	15%	56.9

* Experimental frequency measurement for 570 μm square membrane is 219 KHz

4.5: Effect of combination of thickness and in-plane dimensions variation

In this part of the study, both thickness and in-plane dimensions were varied. Specifically, a +15% of thickness uncertainty is applied on the silicon layer thickness and -15% of uncertainty to the membrane width for the four square plates with the sizes of 570 by 570, 1070 by 1070, 1570 by 1570, and 2070 by 2070 μm. The results are summarized in Figure 22. The combination of variations raises the frequencies from the range of 75.2 - 5.7 KHz to 119 - 9 KHz, but they are still below the experimentally observed range, 219 - 42 KHz.
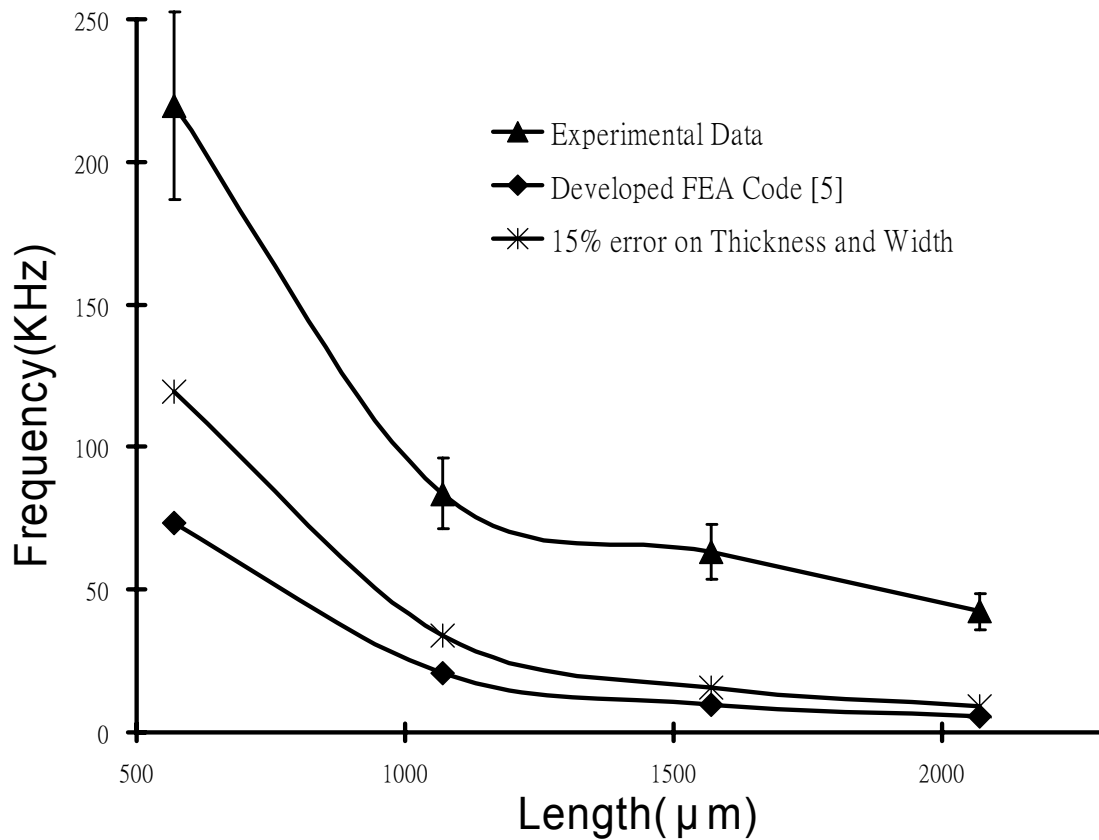
Figure 22: ANSYS flat plate effects of thickness and in-plane dimension variation results compare to experimental data and FEA results.

4.6 Short conclusion:

The developed FEA code and ANSYS has been mutually verified with each other. The verification established a baseline for the study of the effects of dimensional variations on the resonance frequencies. This study focuses on the bigger size of membranes whose widths are greater than 500 μm. Element SHELL99 is chosen to be the type of element used for dynamic modal analysis. The dimensional variations could increase the frequencies by 8% to 20%, but the predicted frequencies were still 45% to 78% lower than the experimental data.

Chapter 5

Effect of shape variation on the resonance frequency

In the calculations described in the last section, the membranes were all assumed to be flat. The calculations showed that the 15% variation of the thickness and in-plane dimensions are not sufficient to raise the calculated frequencies to the experimentally observed levels. It is well known [5] that the membrane shape also has significant effect on the dynamic response of the membrane structures. This effect is investigated in this part of the study. Specifically, three different shapes, namely, dome shape, up-and-down shape, and double-up-and-down shape as shown in Figure23 are investigated.

The levels of the distorted plates can be created by different radii. Fewer radii result in larger displacement in the distorted membrane. For each shape, the resonance frequency increases with the displacement. In this study, the maximum displacement that is required for each shape to reach the experimentally observed frequencies (within 1 %) was calculated. For each shape, the maximum displacement together with its corresponding ratio with respect to the membrane size, and the first three fundamental mode shapes are determined and presented.
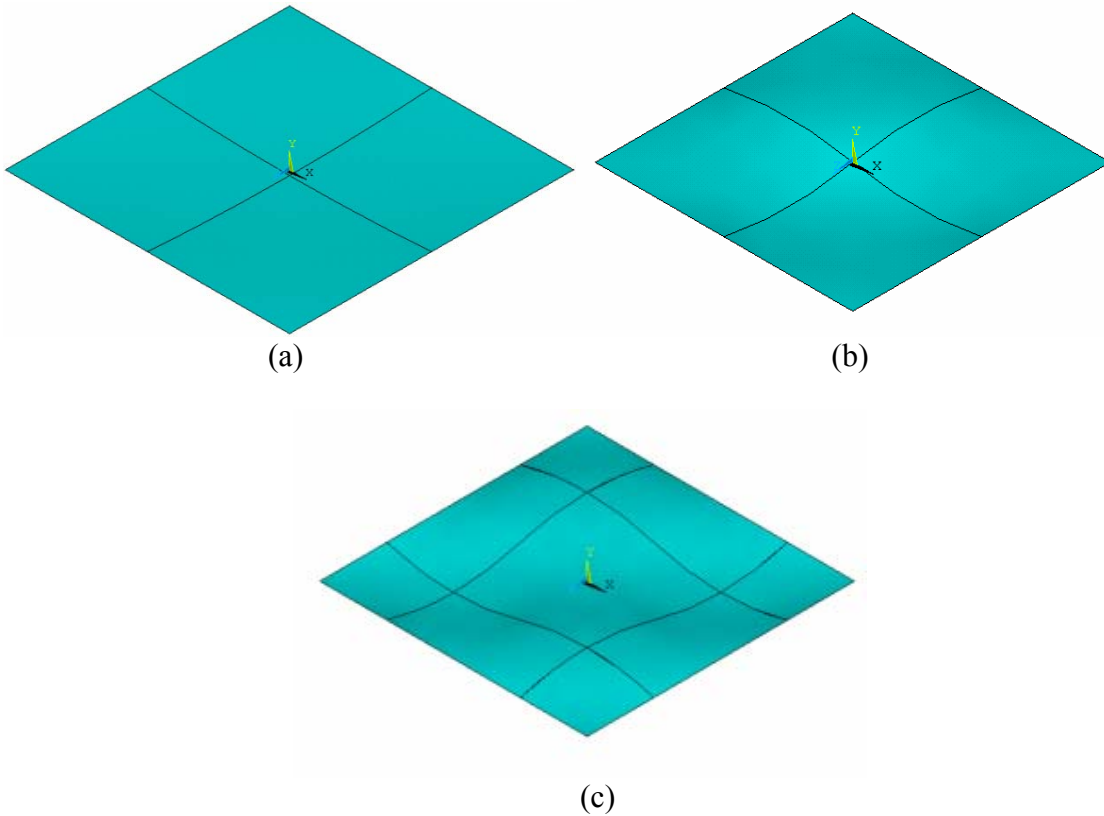
(a)

(b)

(c)

Figure 23: (a) A dome shape plate, (b) up-and-down shapes, and (c) double up-and-down shape

5.1: Element used and its properties

SHELL99 may be used for layered shell structures. The geometry, node locations, and the coordinate system for this element were shown in section3.2.

5.2: Model creation and mesh generation

After the element has been selected, the shape of the membrane can be created by the use of keypoints. Keypoints represent the particular locations placed on the surface. A simple way to create KPs is to use part of circles that pass through the plate domain (Figure24). Keypoints can be selected based on these circles. The curvatures of the final plates are determined by the radius of the circle used. After keypoints are created, the curvature area can be generated by following the instructions described earlier. The material properties were input the same way as stated before. ANSYS identifies each set of material property with a unique reference number. In this part of study, each set of material property includes: Young's modulus, Poisson's ratio, and thickness as presented in Table1. The five sets of material properties can be entered in the material property selection dialog box. ANSYS accesses these properties through these unique reference numbers. The finite element model was created using *solid modeling* method. The created membrane structure was meshed up by applying material properties in each solid layer, setting element size controls, specifying element shape, and meshing type (free or mapped). The analysis type for this part of the study is modal analysis. In boundary condition setting, the primary variables are used, the zero displacements are specified along on the surrounding lines of solid model in accordance with the clamped boundary condition. After the model has been created and boundary conditions have been set, the problem can be solved. After the solution has been obtained, the first three fundamental frequencies and modal shapes can be displayed and reviewed.
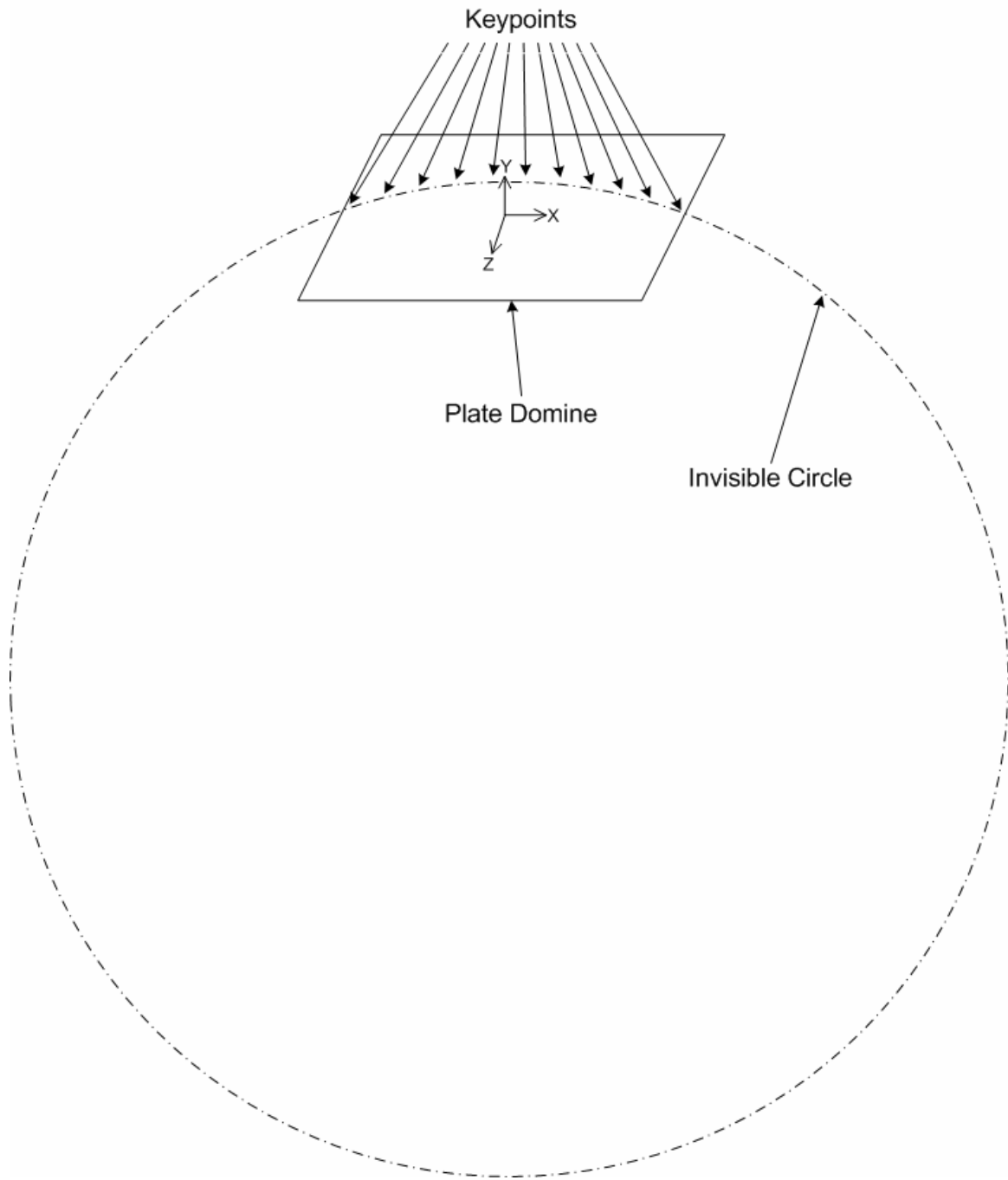
Figure 24: Create keypoints

5.3: Dome shape

To create the dome shape, assume that a ball is placed at the center of membrane domain. Keypoints which are located on the two crossing cycles which are placed at the center of the plate are used to generate the surface domain. Results for the dome-shape plates are shown in Table 4. The table shows that the four sizes of membranes all have similar displacement/size ratios.

(a)

(b)

(c)

43
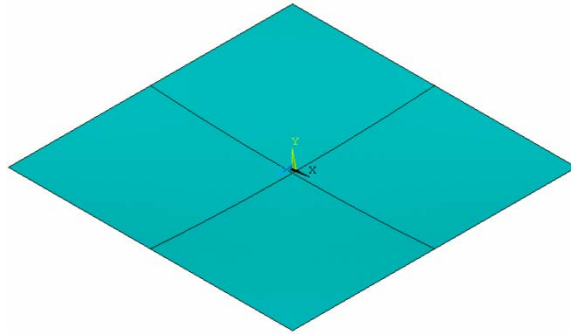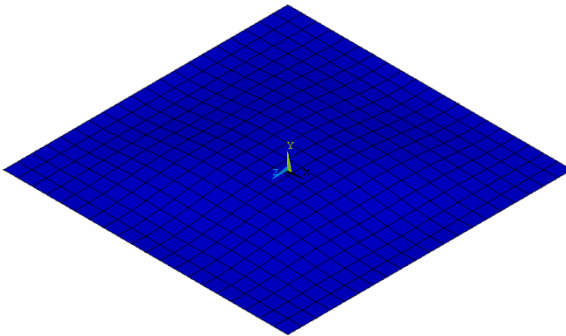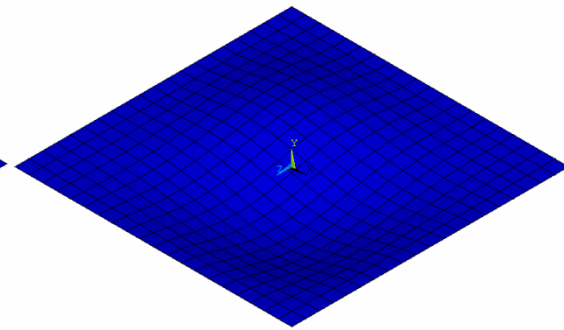
(d)

Figure 25: (a) A dome shape plate, and (b)-(d) first three variation modal shapes

Table 4. ANSYS dome shape frequency results compare to HS experiment results

Membrane size(µm)	Max Dis.(µm)	Ratio(Max Dis./ Membrane size)	Frequency(KHz)	Diff.
570 by 570	10.04	1.8%	219.93	0.15%
1070 by 1070	15.91	1.5%	83.05	0.76%
1570 by 1570	31.49	2.0%	62.98	0.08%
2070 by 2070	43.35	2.1%	42.37	0.23%

5.4: Wavy shape

Two types of wavy shapes were examined: an up-and-down shape and a double up-and-down shape. For the up-and-down shape, assume two balls are placed on the surface. One is attached to the top of the surface and the other to the bottom of the surface along the diagonal direction. Keypoints which are located on the surface can be calculated. Afterward, the surface domain can be generated. Results for the up-and-down shape of plates are shown in Table 5. Compared with the dome shape, the up-and-down shape requires higher displacement-size ratios (greater distortion of the structure) to

44

match experiment data. For this shape, all sizes of membranes again have similar

displacement-size ratios as shown in Table 5.

(a)

(b)   (c)

(d)
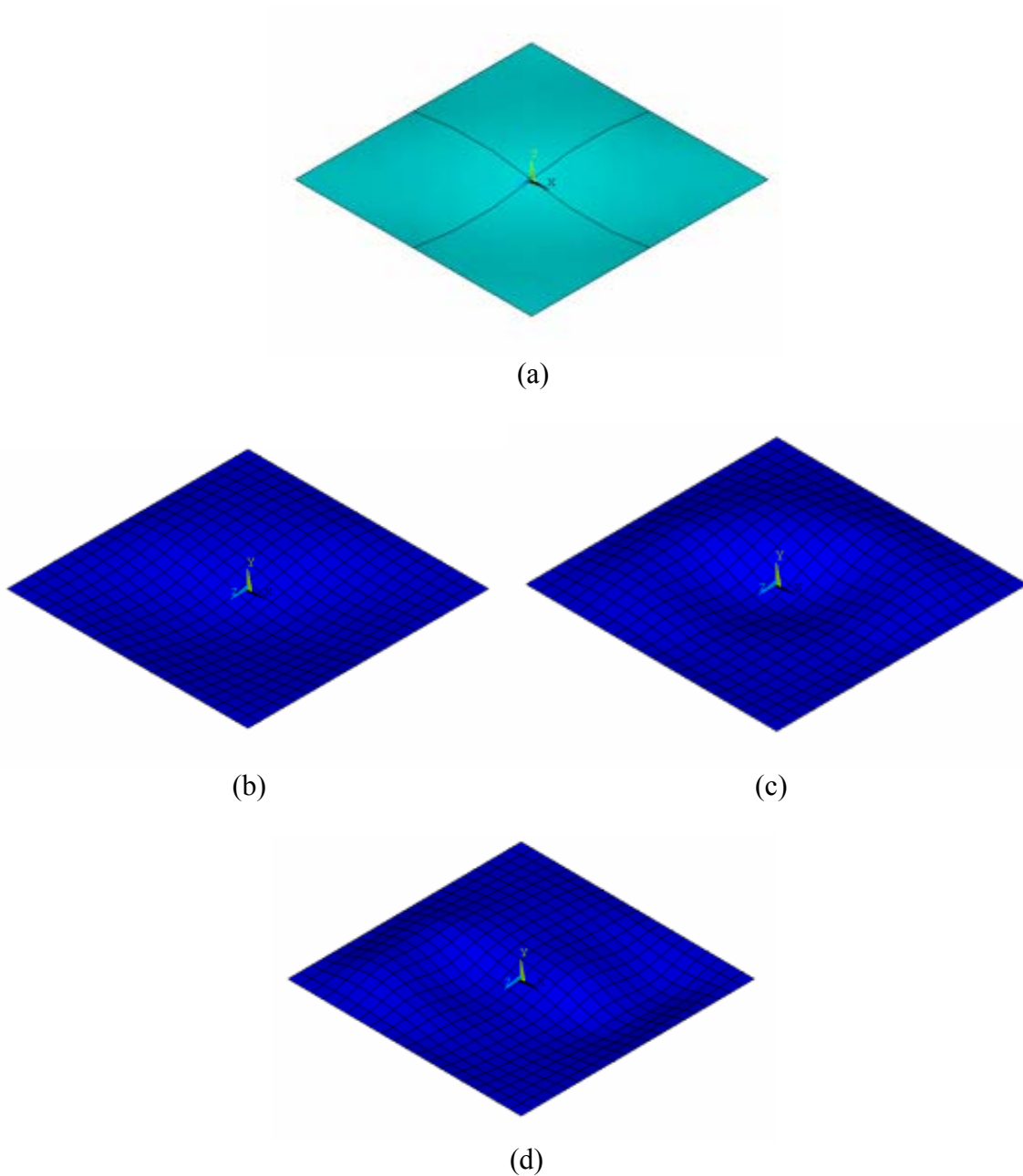
Figure 26: (a) An up-and-down shape plate, (b)-(d) first three variation modal shapes

Table 5. ANSYS up-and-down shape frequency results compare to HS experiment results

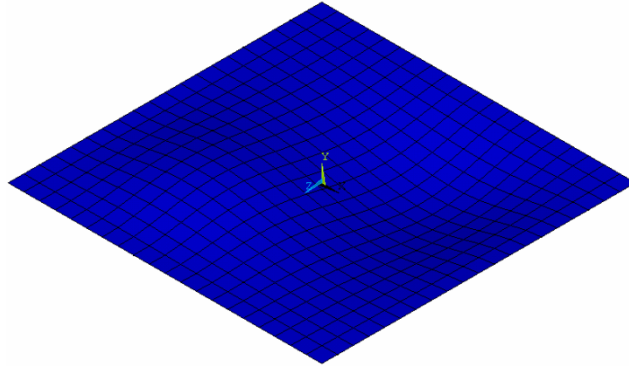| Membrane size(μm)	Max Dis.(μm)	Ratio	Frequency(KHz)	Diff.
570 by 570	17.71	3.1%	218.25	0.34%
1070 by 1070	25.32	2.4%	82.01	0.19%
1570 by 1570	44.11	2.8%	62.98	0.07%
2070 by 20070	52.00	2.5%	42.13	0.81%

For the double up-and-down shape, assume four balls are placed on the surface. Two are attached to the top of the surface and two to the bottom the surface along the diagonal direction. Keypoints which are located in the surface can be calculated. Afterward, the surface domain can be generated. Results for the double up-and-down shape of plates are shown in Table 6. Compared with previous two shapes, this shape requires even higher displacement-size ratio to match the experiment data. For this shape, again all sizes of membranes have similar ratios as shown in Table 6.

(a)

46

(b)   (c)

(b)
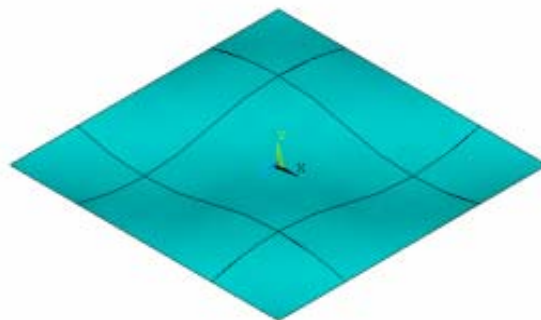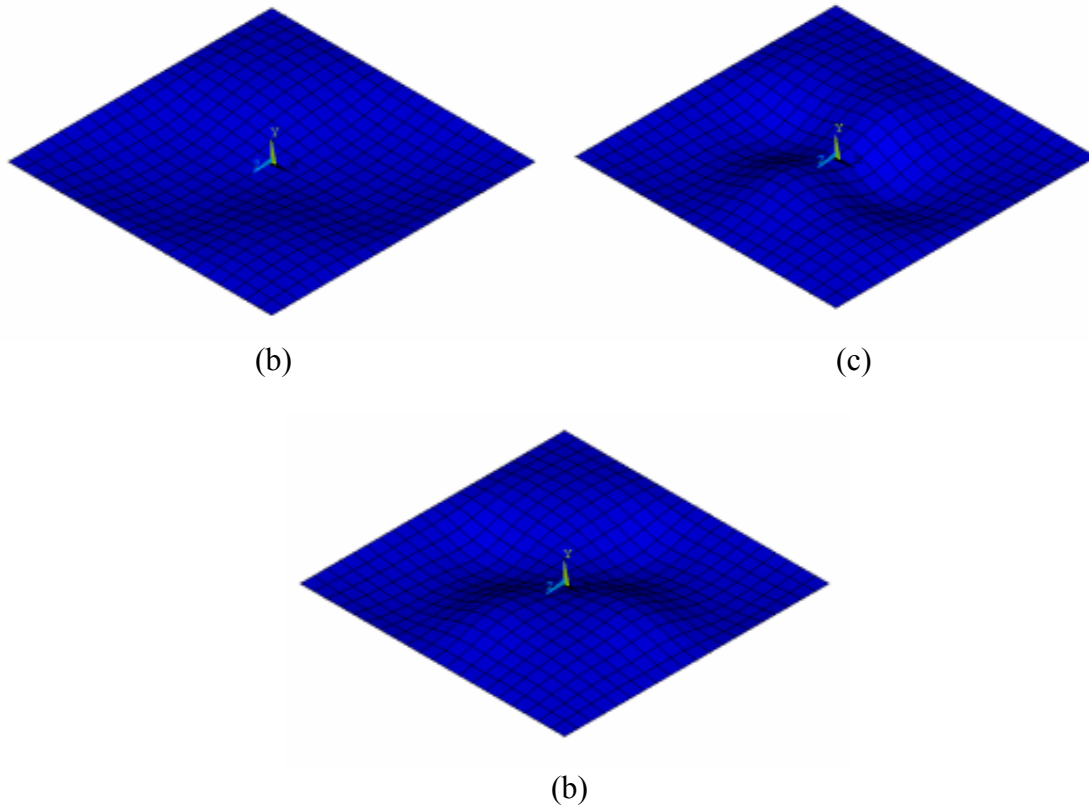
Figure 27: (a) A double up-and-down shape plate, (b)-(d) First three variation modal shapes

Table 6.ANSYS double up-and-down shape frequency results compare to HS experiment results

Membrane size(µm)	Max Dis.(µm)	Ratio	Frequency(KHz)	Diff.
570 by 570	15.21	2.7%	219.67	0.03%
1070 by 1070	22.38	2.1%	83.68	0.01%
1570 by 1570	43.32	2.8%	62.96	0.11%
2070 by 20070	43.38	2.1%	42.61	0.33%

5.5: Short conclusion:

In this part of the study, the effects of membrane shapes on the dynamic response

of the membrane structures were investigated. Membrane structure with curved shape has

higher frequency than the flat plate with the same size. Furthermore, the larger the out-of-plane displacement results the larger the frequencies. Among the three shapes examined, the dome shape has the highest frequency compared to other shape with the same out-of-plane displacement.

Chapter 6

Analysis of residual stress due to thermal mismatch and the corresponding shape

and frequency change

6.1: Source of residual stress

Residual stresses are stresses that are inside or locked into a component or assembly of parts after external stresses or thermal gradients are removed. The origin of residual stresses has been widely studied by many researchers, [23] - [27]. In MEMS fabrication, the thin film deposition is the main fabrication process. Since all deposition processes [23] are kinetically controlled, they are not in thermodynamic equilibrium. The films contain defects that can act as sources of stress. Defects include thermal expansion mismatch between the film and substrate [23-25], phase transformations [23], variation of interaotmic spacing with crystal size [23], incorporation of atoms into the film [24], and recrystallization processes [26,27]. Residual stresses are normally subdivided into two main groups: thermal and intrinsic.

6.1.1 Thermal stress

During the chips fabrication process, subtract and films are prepared and coated at high temperature and cooled down to room temperature. The membrane will be stressed

after the cycling thermal effects. In one-dimension problem, the amount of the stress

cause of the temperature changing can be calculated as follow [23]:

$$\sigma = E\alpha\Delta T$$

6.1

Where α is the linear thermal expansion coefficient, E is the Young's modulus, and ΔT is

the temperature change. For a multilayered structure such as that shown in Figure 28, the

film and substrate stress, when subjected to temperature changing ΔT, can be expressed

as [24], [25].

$$\sigma_{xx} = \frac{E}{1-v^2}\left(\varepsilon_{xx} + v\varepsilon_{yy}\right) - \frac{E\Delta\alpha\Delta T}{1-v}$$

$$\sigma_{yy} = \frac{E}{1-v^2}\left(\varepsilon_{yy} + v\varepsilon_{xx}\right) - \frac{E\Delta\alpha\Delta T}{1-v}$$

6.2

$$\sigma_{xy} = G\varepsilon_{xy}$$

Where σ_{ij} and ε_{ij} are stress and strain components, E, G, and v are the Yong's modulus,

shear modulus, and Poisson's ratio. $\Delta\alpha$ is the difference between the coefficients of

thermal expansion of film and its associated substrate. The contribution of thermal stress

is caused by the constrained thermal strain and is independent to the stress caused by the

applied thermal loading. Assume that all the layers in the multilayered structure shown in

Figure28 are bonded together perfectly. When the temperature is elevated or cooled,

material will expand or shrink in different amount due to differential thermal expansion

ratio in different layers, and the interfacial stress will be developed. Both the thermal treatment (heating or cooling) and restraint of the component must be present in order to generate residual stresses. If the film is under the tensile residual stress, the structure will be deformed into a downward dome shape. On the other hand, the structure will be deformed upward if the film is under compressive stress [23].
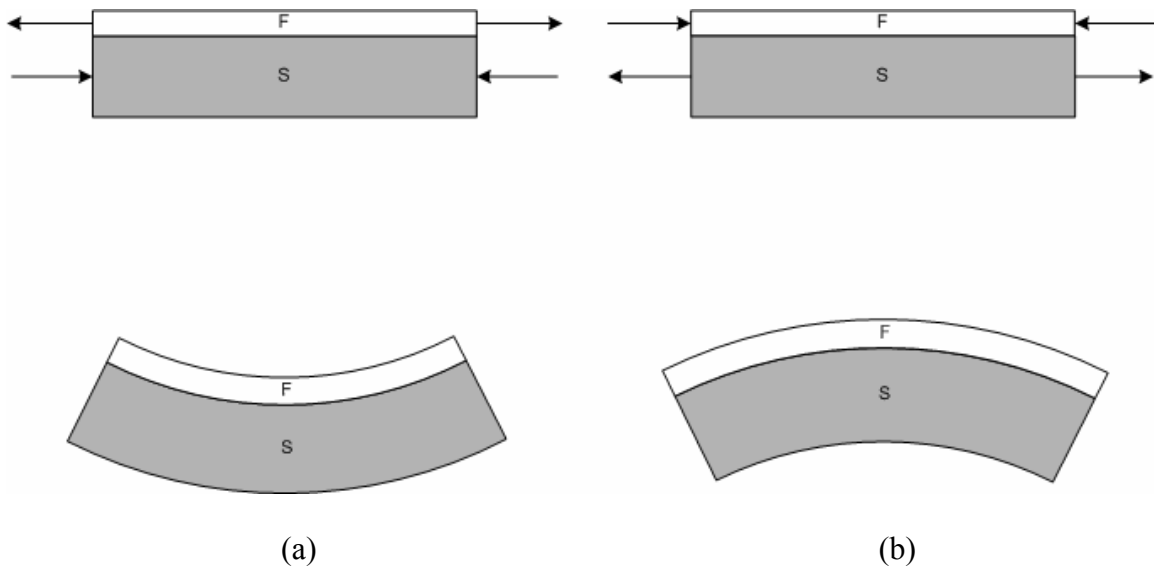
Figure 28: Plate deformation under (a) residual tensile stress and (b) residual compressive stress

6.1.2 Intrinsic Stress

Intrinsic Stress Due to Crystallite Coalescence at Grain Boundaries

During deposition, the crystallites increase their sizes and fill up the small gap between their neighbors (Figure29a.). These crystallites undergo constrained relaxation at the top layer of each surface due to the interatomic forces acting between these gaps

(Figure28b). The stress due to the coalescence of isolated crystallites when forming a

grain boundary can be developed as [23]

$$\sigma = \frac{Y \Delta p}{(1-v)l_g} \qquad (6.2)$$

where l_g is the average grain size, Δ is the constrained relaxation length, and p is the

packing density of the film.

Figure 29: Depiction of grain coalescence [23]

Hoffman [27] and Koc [28] have addressed the issue the tensile stresses are

generated grain boundary relaxation. During deposition, crystallites grow uninhibited

52

until only a small gap separates them from their neighbors and reach their equilibrium position. An elastic strain and a corresponding intrinsic tensile stress are then developed in the film. The residual stress development d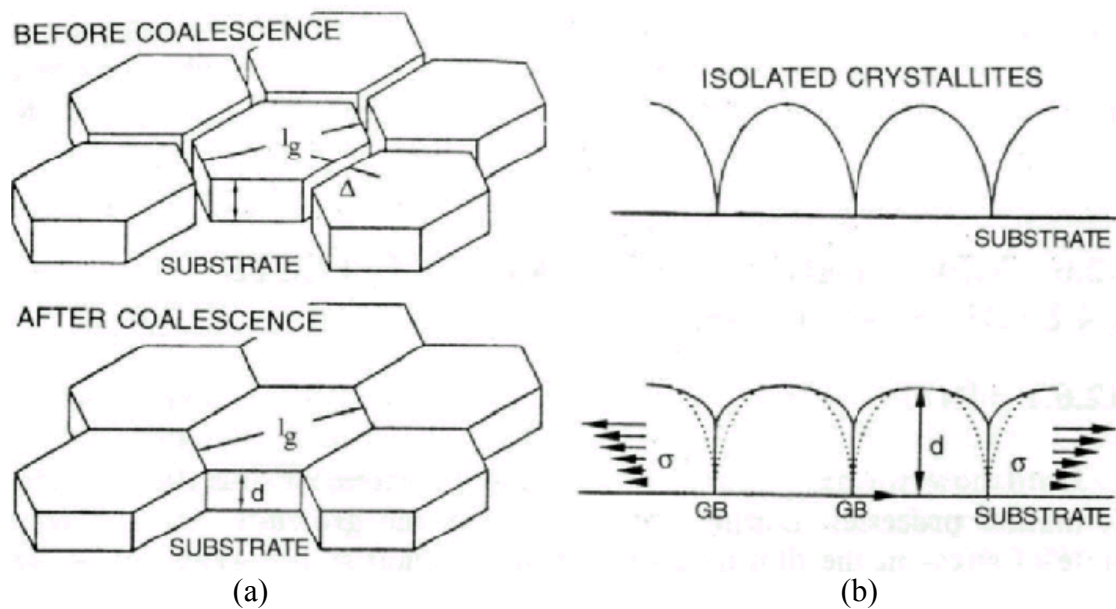uring the coalescence of crystallites and grain boundary diffusion might amplify the structure stiffness and increase resultant frequency.

In addition, Chaundri [29] has addressed two mechanisms that are likely to contribute to tensile stress generation during coalescence. The first involves grain growth by eliminating grain boundaries. The normal lattice is increased slightly, and this distortion induces tensile residual stress. The second process that may produce tensile stresses in the film involves the filling and closure of channels and holes. It is generally observed that film deposited at low temperature usually exhibited a significant amount of tensile residual stress after a subsequent thermal loading [30]. That is because that the porous microstructure forming at low temperature deposition can be eliminated by a high temperature thermal cycling process and this induces tensile residual stress.

Intrinsic Stress Due to Recrystallization Effects

In metal films, recrystallization can be a large contributor to the intrinsic stress. Recrystallization can occur both while the film is deposited and after completion of the deposition if the material's self-diffusion is high [26]. During film deposition at elevated temperatures, disordered material behind the advancing film surface is annealing, causing the film thickness to shrink and the grains to grow. This stress occurs when the rate of monolayer growth is faster than the thermally activated atom movements to recrystallize

53

the surface. This densification leads to a tensile film stress. The decrease in grain

boundary area by increasing the average diameter from an initial diameter, D_0, to the final

grain size, D, leads to a stress of recrystallization, σ_{recr}. [26]

$$\sigma_{recr} = \frac{2E}{1-\nu} \Delta \upsilon_{ex} \left(\frac{1}{D_0} - \frac{1}{D} \right) \qquad (6.3)$$

where E is the film modulus, υ is the Poisson's ratio, and $\Delta \upsilon_{ex}$ is the volume being

considered. Although this equation models this process well, it excludes all other stress

generation mechanisms such as small-angle grain boundaries [26].

Intrinsic Stress Due to Boron Diffusion

Finally, one more possible source of residual stress is the boron diffusion. In this

process, the boron atoms are squeezed into the silicon crystal in an incompatible manner.

This results in some tensile residual stress and increased stiffness of the silicon film. The

increased stiffness would result in an increase of frequency.

6.2: Simulation of residual stress due to thermal mismatch

In the references, Nejhad [31] has mentioned that the residual stresses develop

due to extrinsic strains can be determined by using thermal expansion coefficient,

material properties, and processing conditions. The resultant frequency is affected by the

54

thermal stresses and membrane shape deformation [32]. In this part of the study, the

residual stress due to the thermal cycling is investigated using ANSYS. The study

consists of two steps: namely, static analysis and dynamic modal analysis. In the static

analysis, the multilayered structure as shown in Figure 2 is subjected to a thermal cycling

of 25-1000-25 ºC and the resultant deformed shape, residual stresses, and interface

stresses are determined. In order to generate some permanent or locked-in thermal strain,

the yield strengths are input as part of the material properties. In other words, each layer

behaves as an elastic-plastic material, instead of a simple elastic material. In the dynamic

analysis, the deformed shape from the static analysis is used as the input to study its

corresponding dynamic response. As demonstrated earlier, the membrane structures with

curved shapes have higher frequencies than the corresponding flat structure of the same

size.

6.2.1 First step: Obtaining the deformation by thermal loading

The structure to be analyzed consists of five layers, both 2-D and 3-D analyses

were performed. The sketches of the 2-D and 3-D models are shown in Figures 29 and

Figure30, respectively. The layer thicknesses follow those presented in Table 1. The

details of these analyses are described in following sections.

6.2.1.1 Elements used and their properties

PLANE42 is used for 2-D modeling and SOLID45 is used for the 3-D modeling of solid structures. The geometries, node locations, degree of freedoms, and the coordinate systems for both element types were described in section 3.2.

6.2.1.2 ANSYS preprocessor

After the element types have been chosen, the analysis geometries for 2-D and 3-D solid models need to be created and their boundary conditions and coordinates are shown in Figure30 and Figure 31, respectively. Both 2-D and 3-D solid models were created in a flat solid multilayer structure by keypoints. The model creation instructions were interdicted in Chapter3. ANSYS accesses five sets of material properties through the unique reference numbers. In this part of study, each set of material property includes: initial temperature (25ºC), Young's modulus, Passion ratio, yield stress, and thermal expansion coefficient which were presented in Table1. The finite element model was created using *solid modeling* method. The model is meshed by identifying material properties reference number in each solid layer on the working plane, indicating element size controller to let each side of finite element cubic close to1-to-1 and 1-to-1-to-1 ratio, for 2-D and 3-D, respectively, specifying element shape (rectangular), and meshing type (free or mapped). The type of the analysis is static analysis. In thermolmechanical analysis, a prescribed temperature of $1000\,^{\circ}C$ was specified on all created areas and volumes and clamped boundary condition was used. After the solution is obtained, the deformed shape and the stress distribution along the selected paths can be reviewed. The instruction for setting up the path was given in Chapter3. The nodal coordinate and nodal

56

displacement for each node can also be retrieved from ANSYS. These two outputs have to be combined together to generate the deformed shape used for next analysis.
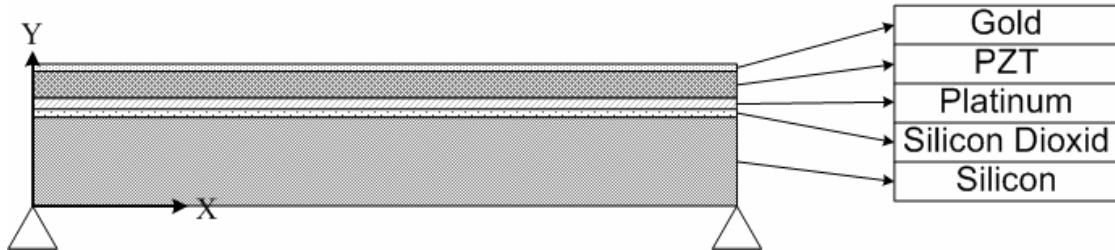

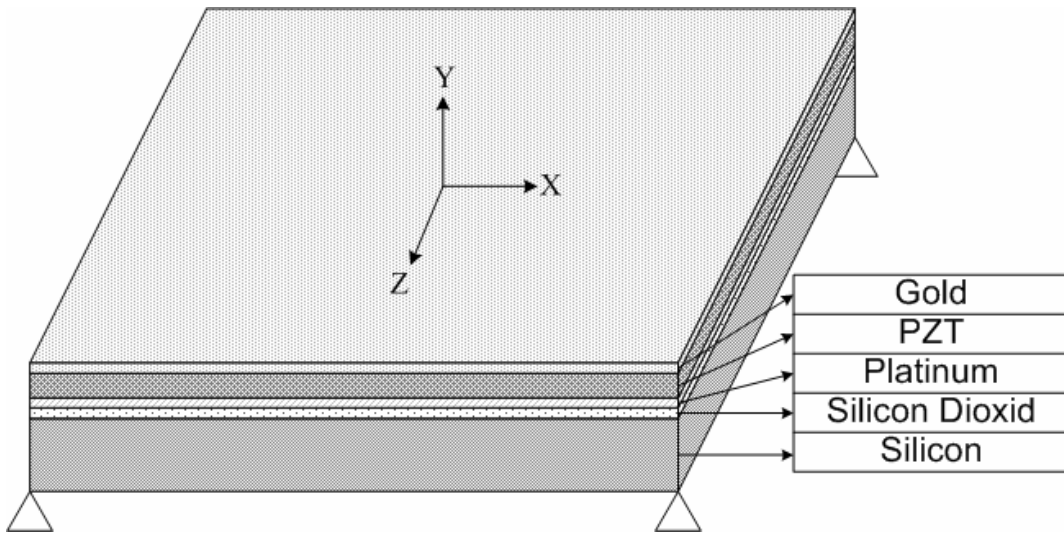**Figure 30: 3-D multilayer structure model for ANSYS plate model for ANSYS**

Figure 31: 3-D multilayer structure solid model for ANSYS plate model for ANSYS

Creating an ANSYS readable input file

In order to increase the processing efficiency and reduce human input errors, MATLAB is used to generate ANSYS code in .lgw file. The .lgw input file contains ANSYS readable code which includes element type (PLAN42 or SOLID45), material properties (present in Table1), reference temperature (25ºC), commands which were used to generate a solid multilayer structure, analysis type (static), and boundary conditions (clamped). The data input was done by the developed input file. An example of code commands is shown in appendix. The flow diagram is shown in Figure 42.

6.2.1.3 Deformation Shapes in 2-D and 3-D models

The deformed shapes due to thermal loading are shown in Figure32 and Figure33 for 2-D and 3-D models, respectively. Both models show a downward dome shape.

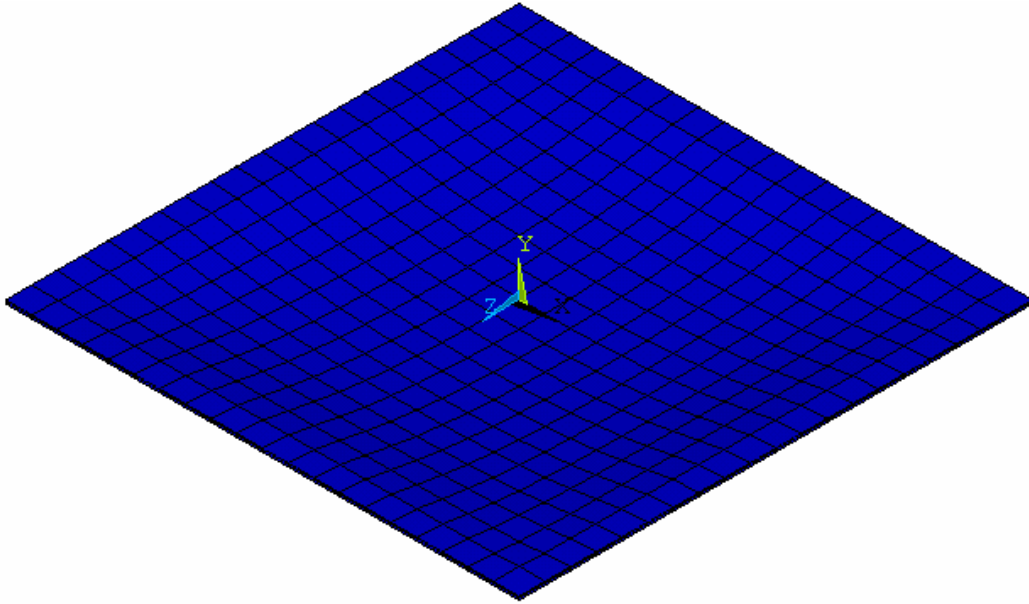
Figure 32: 2-D model deformation

Figure 33: 3-D model deformation

6.2.1.4 Stress Distribution

2-D model

After the solution has been obtained, the stress distribution in the structure can be reviewed. When the thermal loading is applied on the structure, the material will expand and push the boundary. That is the reason why a compression stress in y direction appears on the side boundary (Figure 34 & Figure 35). Recall that for the clamped boundary condition, the primary variables, i.e. displacement and rotation, along the boundary are specified as inhibitive. Furthermore, as the plate is deformed down-ward, the area around the boundary carries most of bending. Accordingly, the largest tensile stress in y direction appears in the area around the boundary (Figure 35). Figure 36 shows the Von Mises

stress distribution at the right corner of multilayer structure, and Figure 37 shows the stress distribution at the center point across the layers along the vertical direction. The stress is highest at the bottom layer and decreases towards the top layer. The SiO$_2$, Gold, and Platinum layers have less stress compared to other layers. According to the plot and discussion in section 6.1.1, the resultant tensile stress placed in the film would result in a downward deformation shape in the multilayer structure.
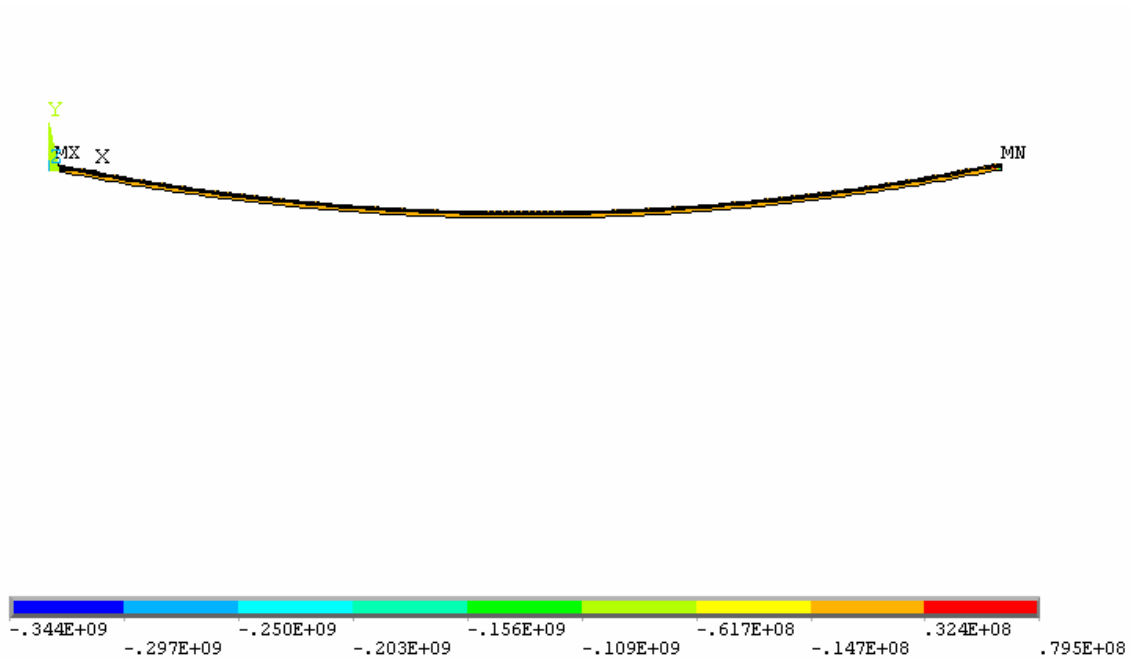

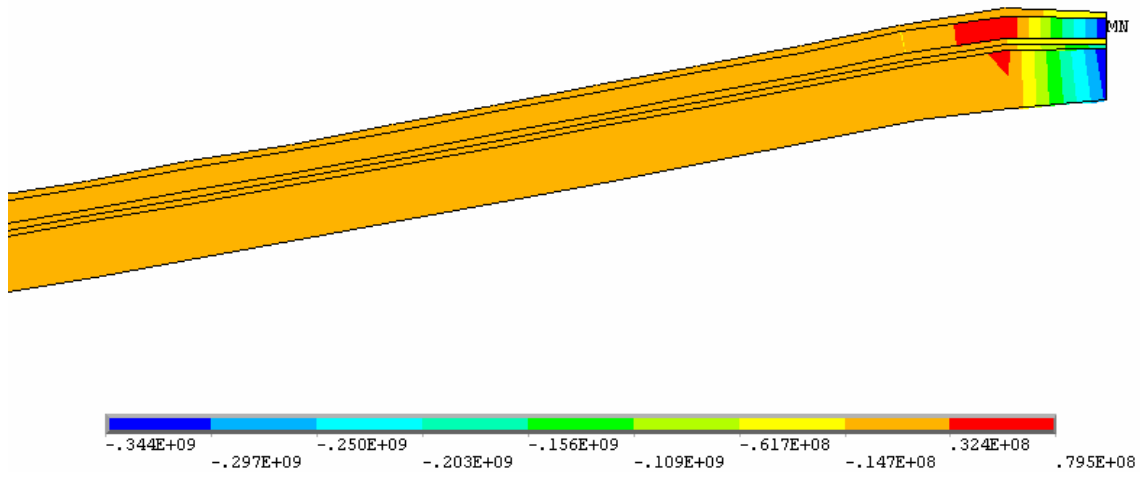**Figure 34: 2-D deformation and stress distribution**

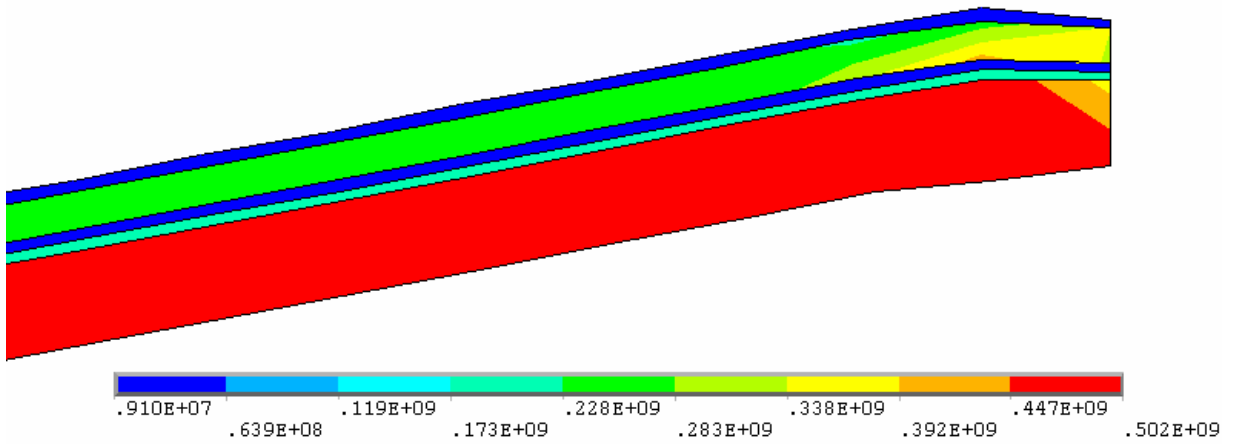**Figure 35: Stress in y direction at right end corner in 2-D model.**

Figure 36: Von Mises stress distribution at right end corner in 2-D model
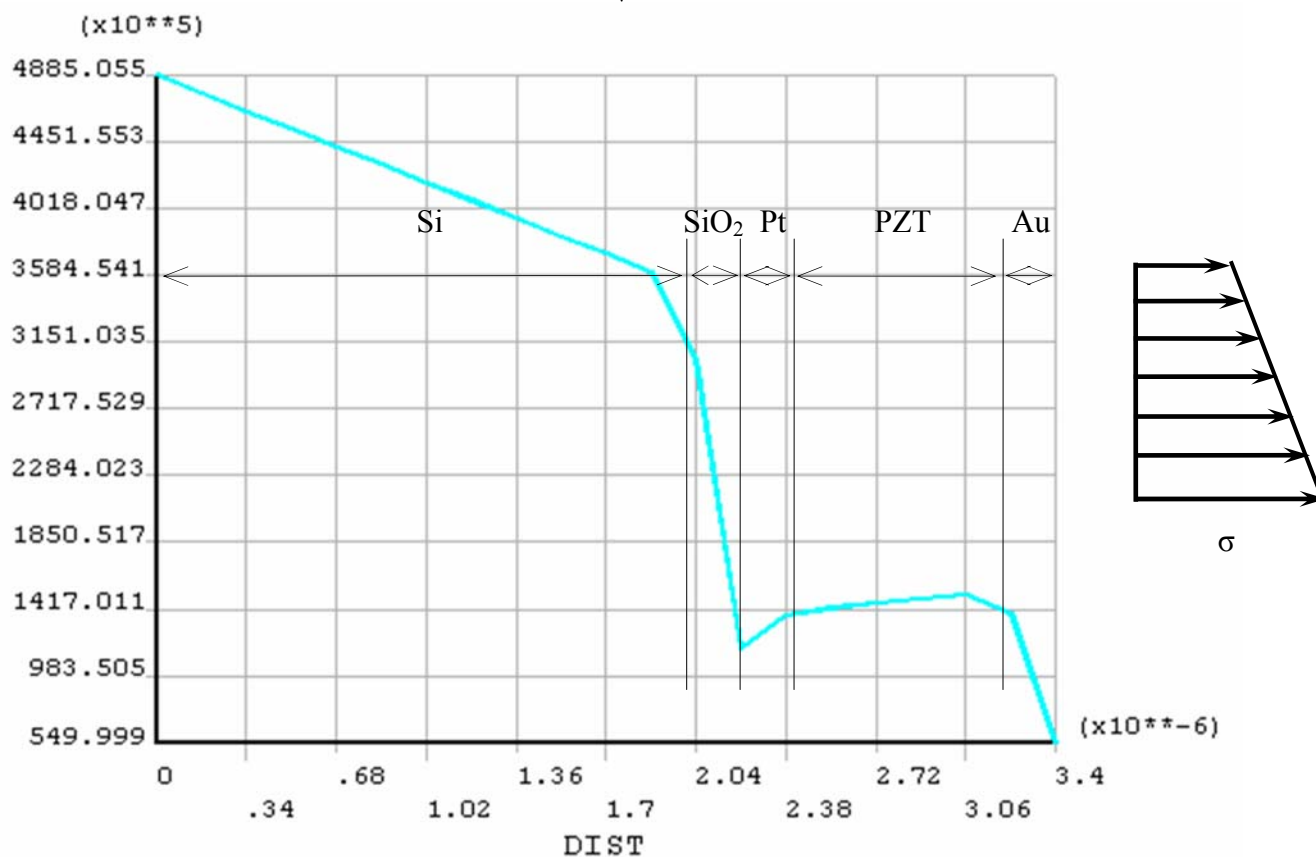
Figure 37: Von Mises stress distribution cross from bottom layer to top layer at center point in2-D model

3-D model

The stress distribution in the 3-D model can be reviewed in three different ways: overall view of on the whole domain (Figure 38), longitudinal view (Figure 39), and transverse view(Figure 40).The Von Mises stress distributions in the plate as viewed from top and bottom are shown in Figure 38 (a) and (b), respectively. The whole plate is under tensile stress and deforms into a downward dome shape. The bottom layer (Silicon) has greater bending radius and carries higher tensile stress than the top layer (Gold).

Figure 39 shows the stress distribution in different interfaces across the corners A and B: top surface (top surface of the gold layer), Interface#1 (gold and PZT layer), Interface#2 (PZT and platinum layer), Interface#3 (platinum and silicon dioxide layer), Interface#4 (silicon dioxide and silicon layer), and bottom surface (bottom surface of silicon layer). Figure 40 (a)-(f) shows the stress distribution in each interface. As shown in Figure 38a, the area along the boundary has face-down curvature and the middle area has face-up curvature. Most of tensile stresses were observed along on the surrounding boundary and middle area. The region which has less tensile stress is the transition area which has less degree of bending between two different directions of bending (Figure 40a). Figure 38b and Figure 40f show the stress distribution on the bottom of the plate. Since the clamped boundary condition has been set, the primary variables, displacement and rotation, along on the boundary are specified as inhibitive. The area around the boundary has less degree of bending and carries less magnitude of tensile stress. Four spots on the bottom of plate are the transition between two different directions of bending and carry less bending resulting in less tensile stress.

Figure 41 shows the stress distribution at center point throughout the layers. The bottom of SiO_2 layer has the highest compressive stress and decrease across the thickness to the top of silicon dioxide layer. The stress increases in platinum layer and continually rises up in PZT layers. Finally, the compressive stress decreases in gold layer and the lowest stress appears at the top of the structure. Both 2-D and 3-D models have similar compressive tress distribution in terms of Von Mises stress, but 3-D stress is 0.2G Pa higher than 2-D.

.300E+08   .145E+09   .260E+09   .374E+09   .489E+09
      .874E+08   .202E+09   .317E+09   .432E+09   .547E+09

(a)

(b)
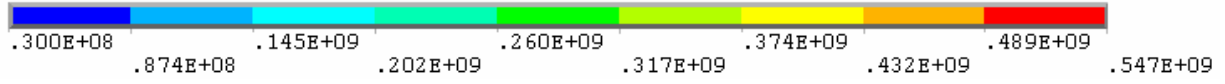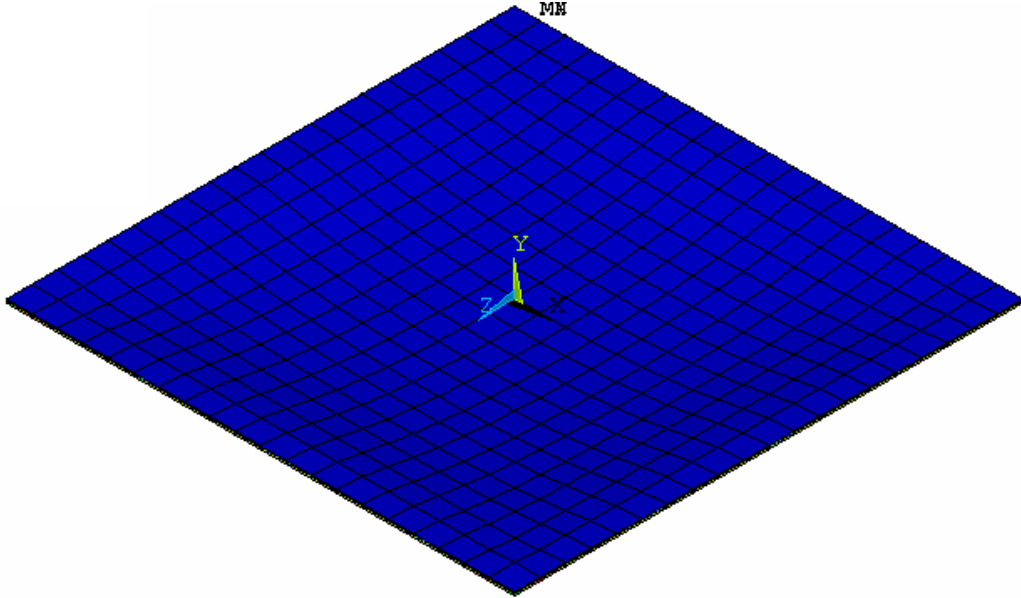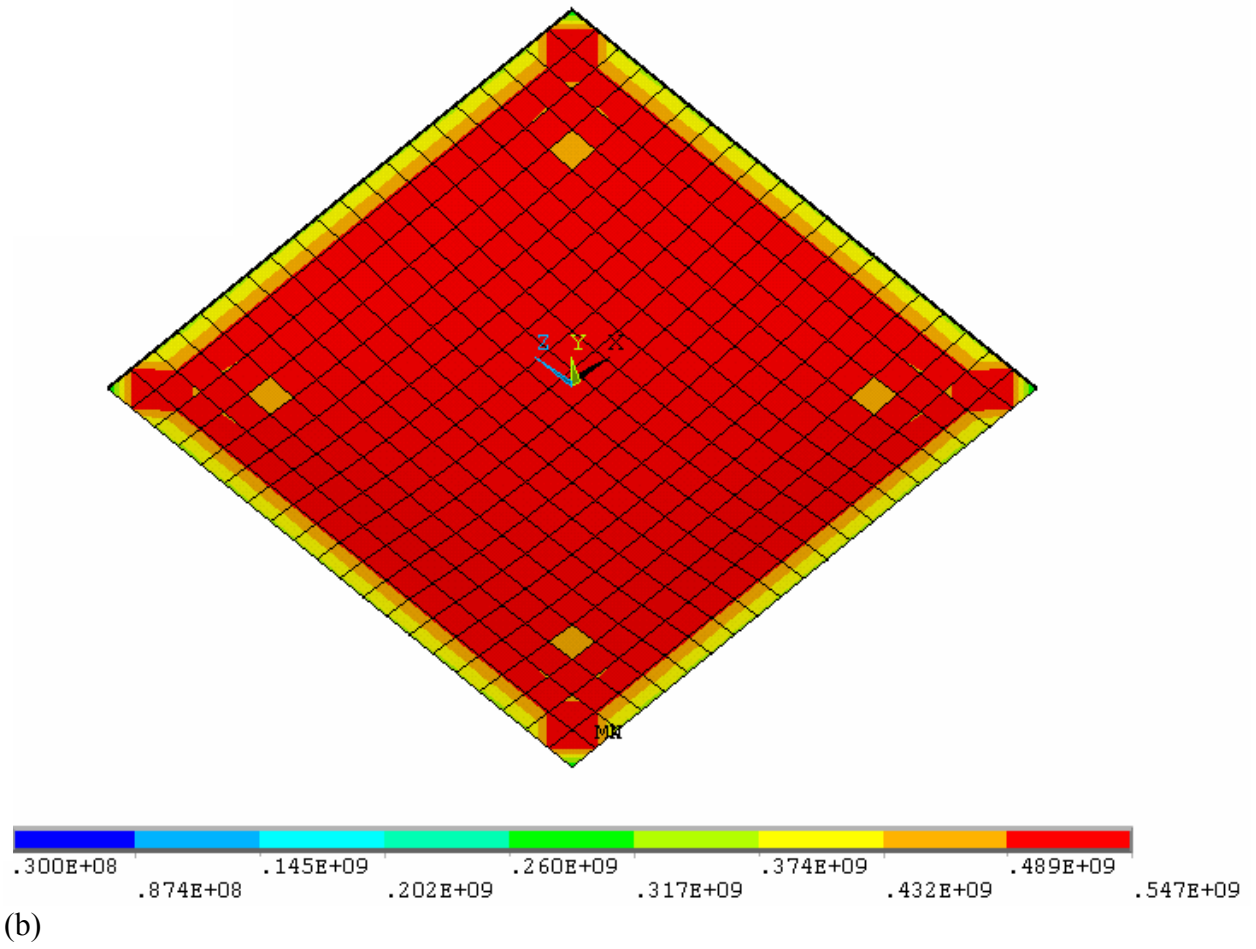
Figure 38: Von Mises stress distribution from (a) top and (b) bottom view
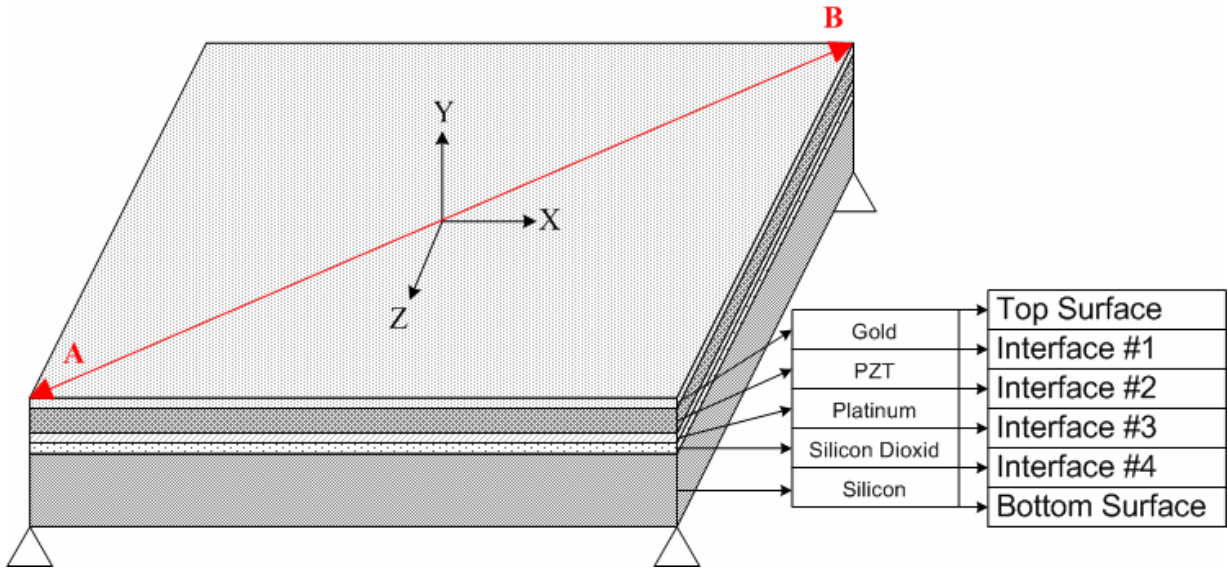
Figure 39:Depiction of interfaces

Stress (Pa)(x10**4)

(a)   Top Surface (Gold)

66

Stress (Pa)(x10**5)
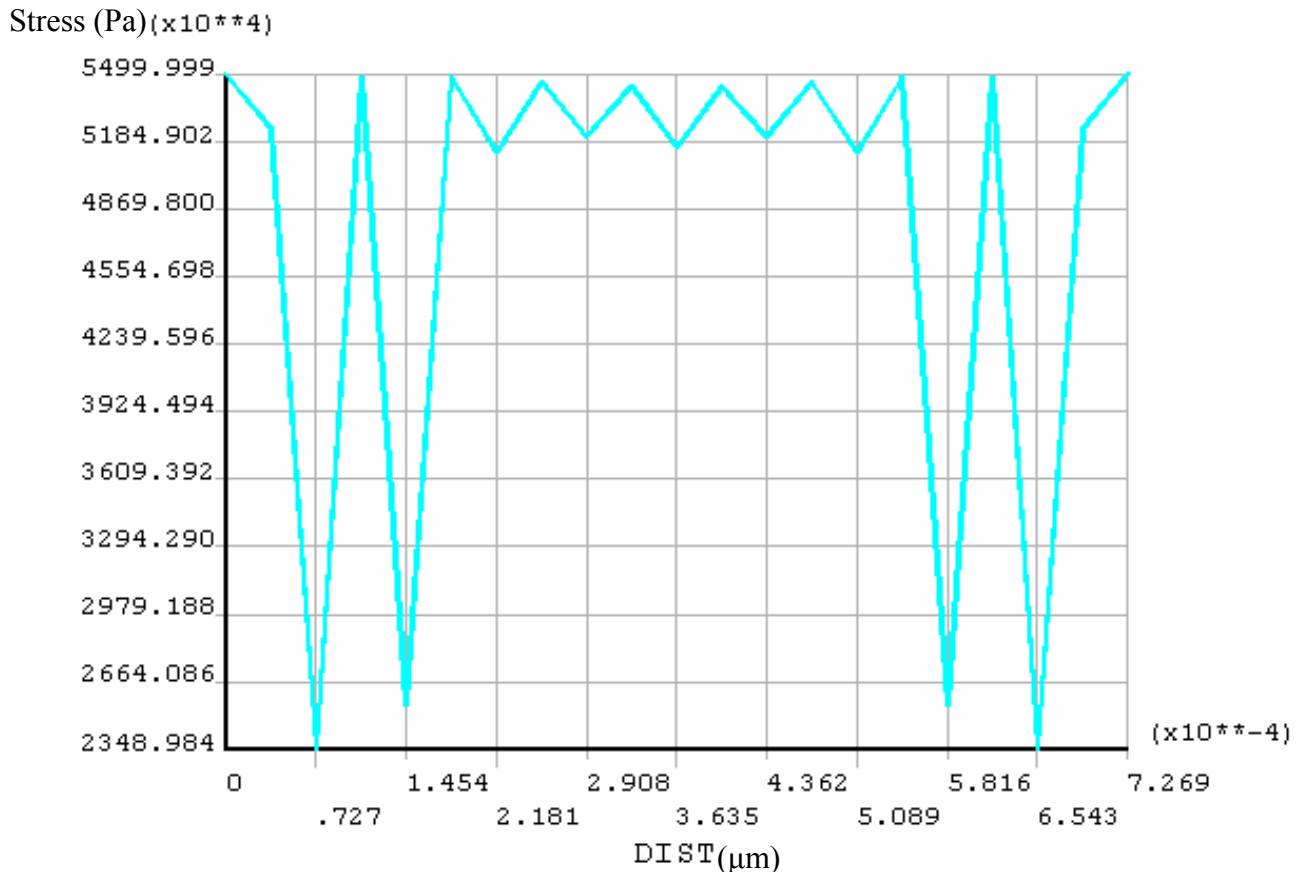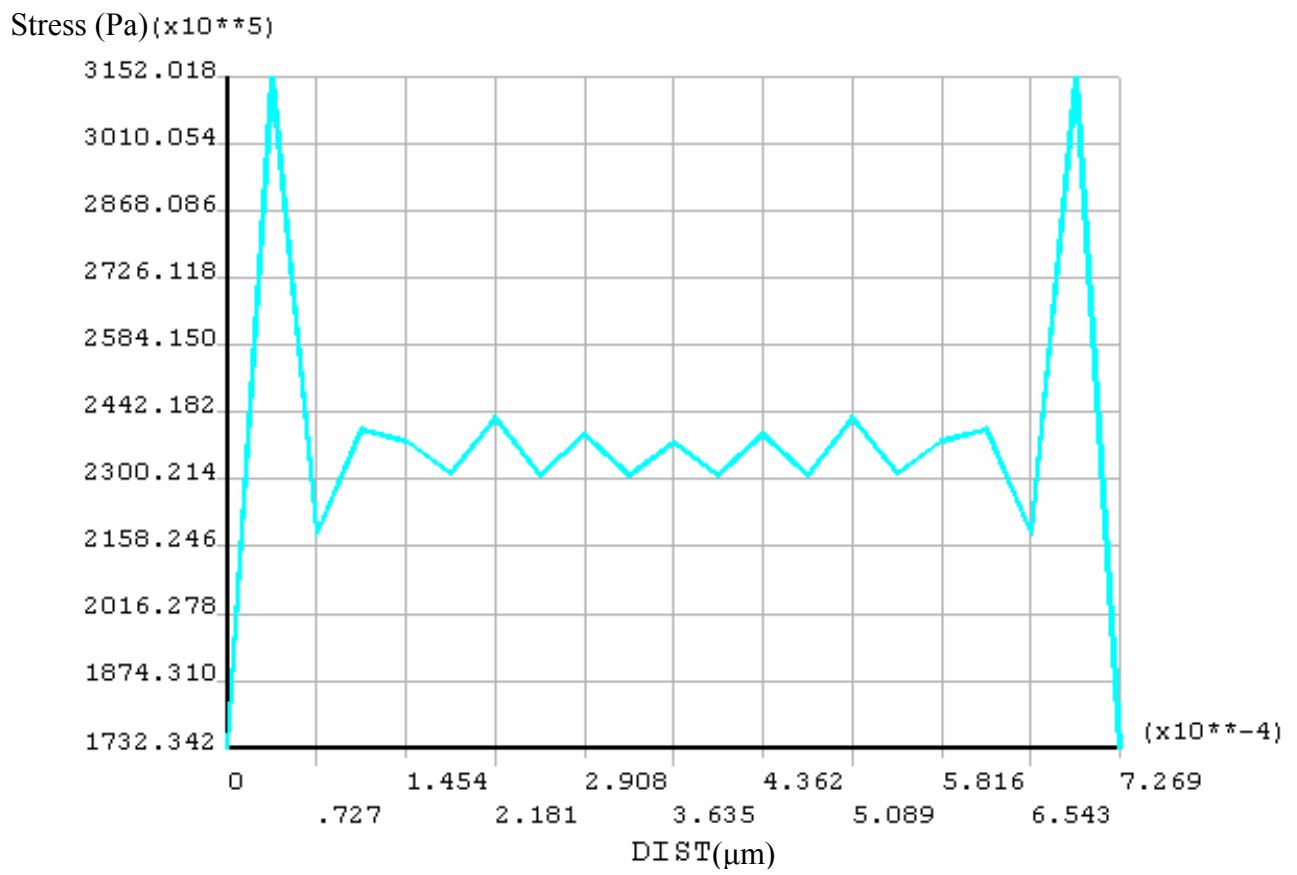
(b) Interface #1 (Gold and PZT)

(c) Interface #2 (PZT and Platinum)

Stress (Pa)(x10**5)

(d) Interface #3 (Platinum and Silicon Dioxide)

Stress (Pa)(x10**5)
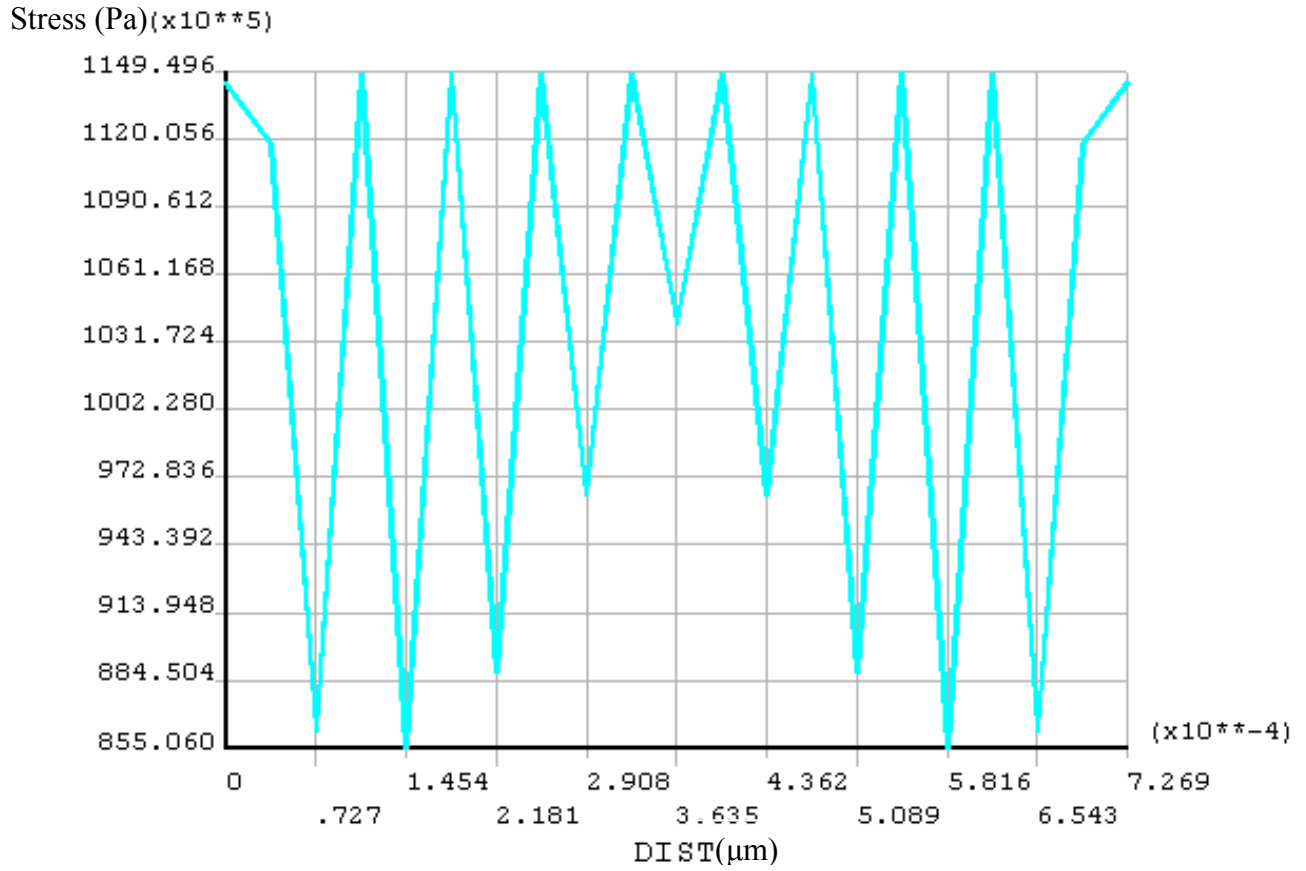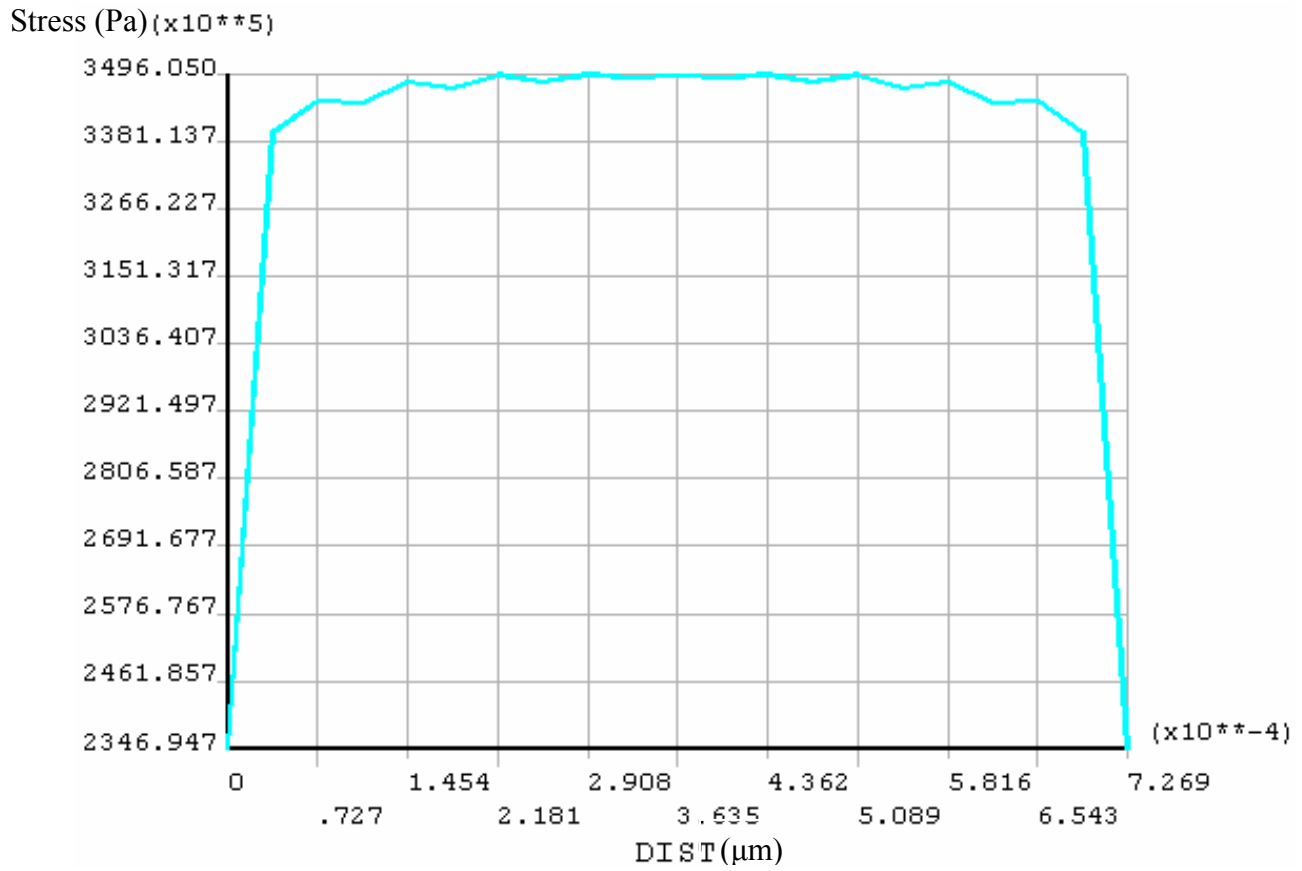
(e) Interface #4 (Silicon Dioxide and Silicon)

Stress (Pa)(x10**5)
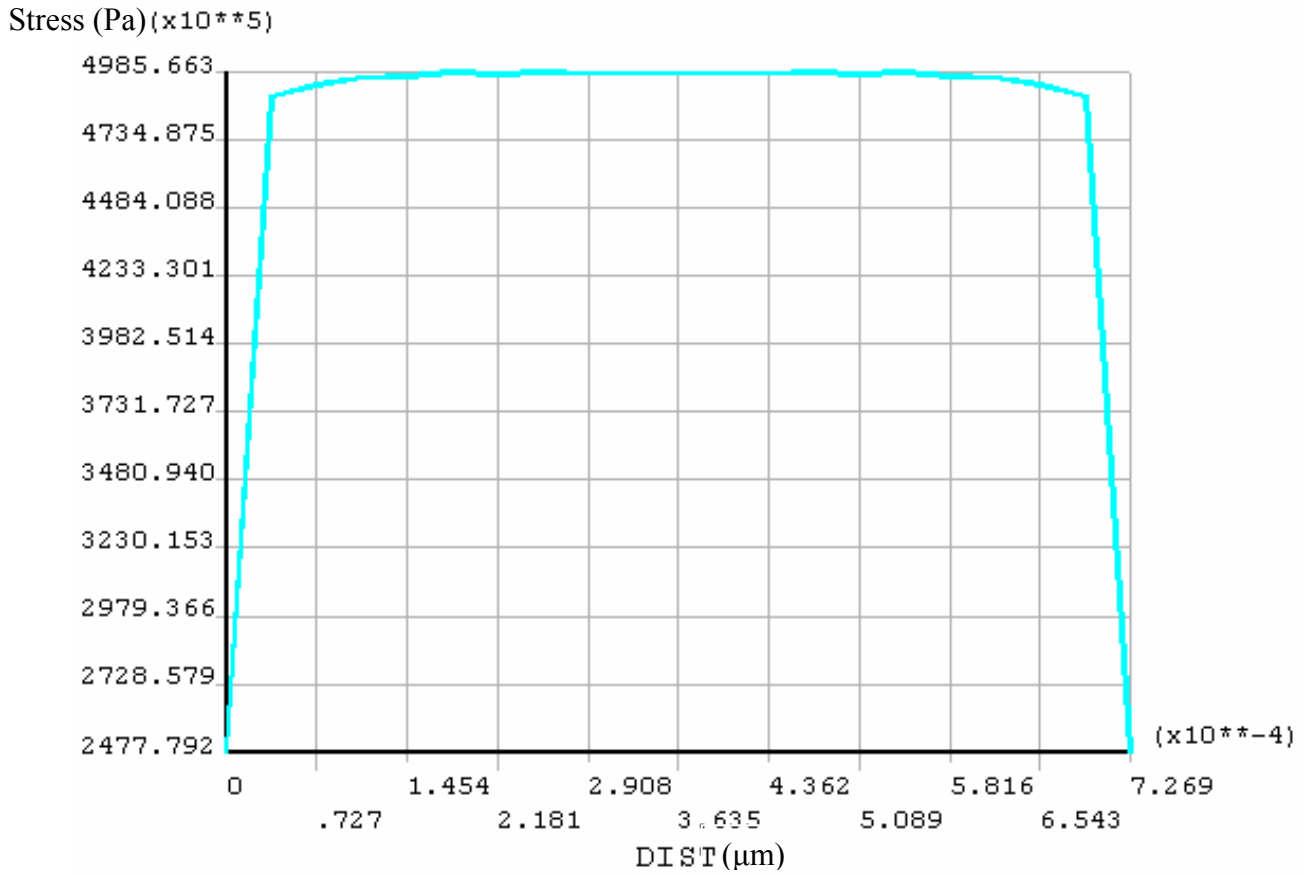
(f) Bottom surface (Silicon)

Figure 40 Interface stress distribution (a) Top surface , (b) Interface #1, (c) Interface #2, (d) Interface #3, (e) Interface #4, and (f) Bottom surface

71
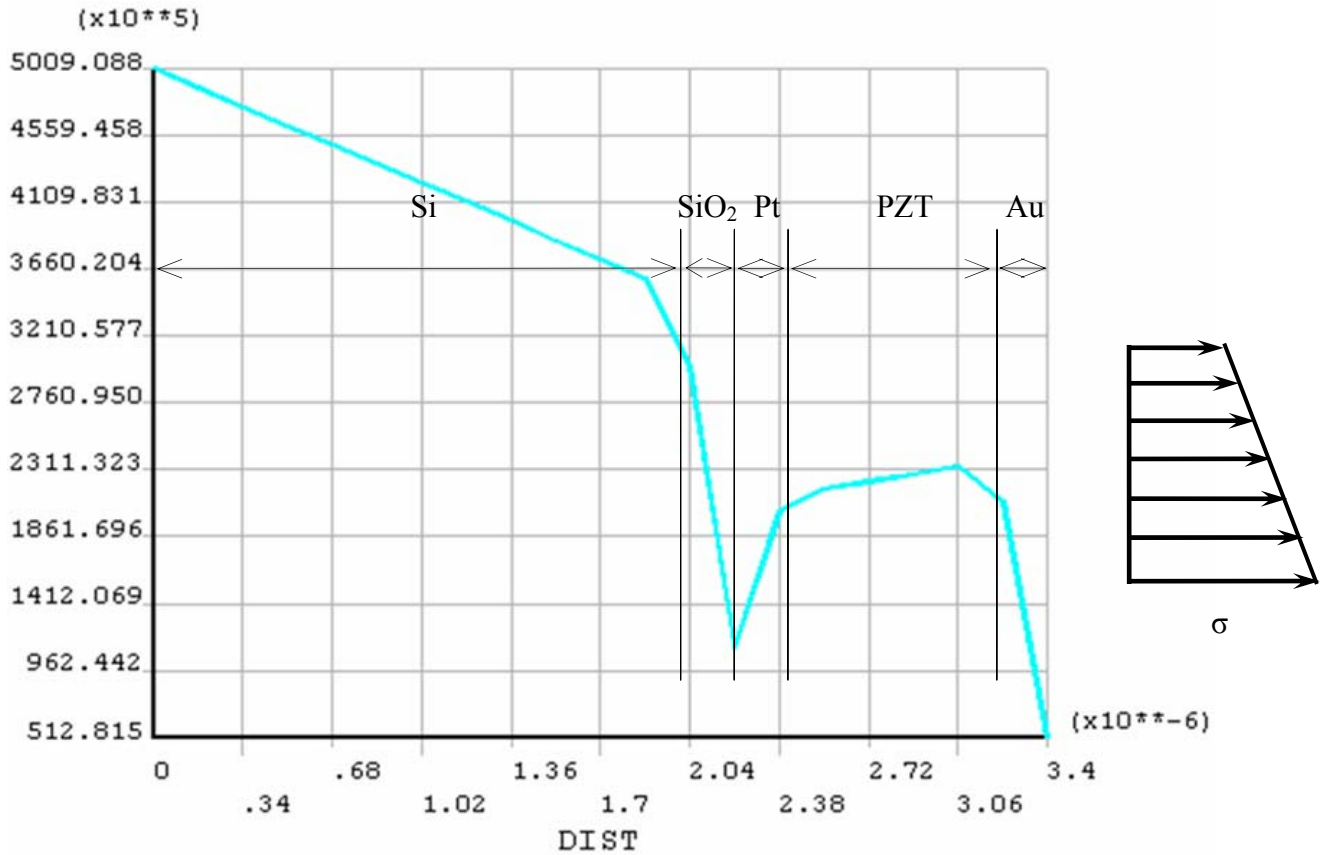
Figure 41:Von Mises stress distribution cross form bottom layer to top layer at center point in 3-D model

6.3: Frequency change due to shape change resulting from thermal mismatch

6.3.1 Second step: Frequency analysis

The second step of the simulation is to obtain the resultant frequency based on the distorted shape from the thermal loading simulation. SHELL 99 element was used in this part of the study. The first step was to generate new keypoints using the nodal coordinates and nodal displacements that were generated from the thermal loading simulation. After keypoints are created, the function "*spline thru KPs*" is used to create

lines by connecting the selected kepoints. Afterwards, areas are created by the selected

lines in either clockwise or counterclockwise direction. Finally, the whole plate model is

generated using "*glue*" command to join all single areas that were created. The material

properties were input the same way as described earlier. The finite element model was

created using *solid modeling* method and by selecting element type SHELL99 as meshing

geometry, identifying material properties reference number in each solid layer with

thickness, indicating element size controller to let each side of finite element model have

a 1-to-1 ratio, specifying element shape (rectangular), and meshing type (free or mapped).

The analysis type for this part of the study is modal analysis. In boundary condition

setting, the primary variables that are inhibited are specified along on the surrounding

lines of solid model as a clamped boundary condition. After specifying the boundary

conditions, the type of analysis to be performed, and the number of modal shapes to be

obtained, the problem is fully defined and solved by ANSYS.

Creating an ANSYS readable input file

For the same reasons described earlier, MATLAB was used to generate ANSYS

code and saved as .lgw format file. T .lgw file contains ANSYS code which includes

keypoints, element type (SHELL99), material properties (present in Table1), commands

to generate a surface structure, boundary conditions, and analysis type. The flow chart for

the overall analysis is shown in Figure 42.
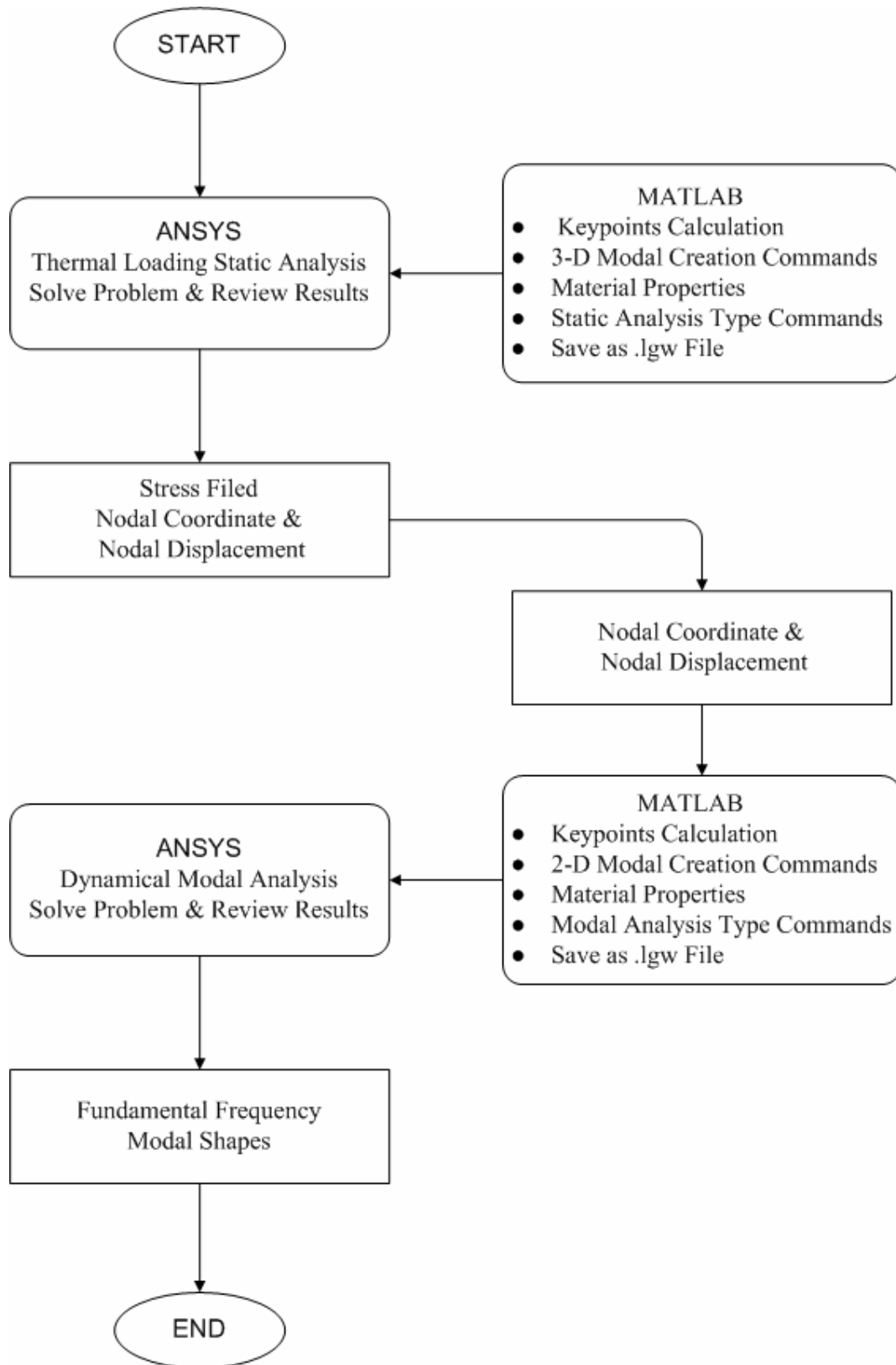
Figure 42: Flow chart of thermal loading variation test

The maximum displacement from the thermal cycling simulation and the first fundamental frequencies from the subsequent modal analysis are listed in Table7. Since the distorted membrane has a dome shape, the maximum displacements and fundamental frequencies are compared with the results listed in Table 4 and experiment data. The results are shown in Table 7and Figure 43, which show that thermal cycling simulation only generates about one-third of the displacements listed in Table 4. The frequencies which are in the range of 75 KHz to 5 KHz obtained from the developed code [5] are increased to the range of 119 KHz to 13 KHz. However, they are still below the experimentally observed range, i.e. 219 KHz to 42 KHz.

Table 7.ANSYS thermal loading plate frequency results compare to HS experiment results

Membrane size(μm)	Max Dis.(μm)	Ratio(Max Dis./ Membrane size)	Frequency(KHz)	Diff.
570 by 570	3.92	0.69%	119.15	45.74%
1070 by 1070	6.13	0.57%	44.75	46.53%
1570 by 1570	6.96	0.44%	22.77	64.03%
2070 by 20070	7.30	0.35%	13.61	67.96%
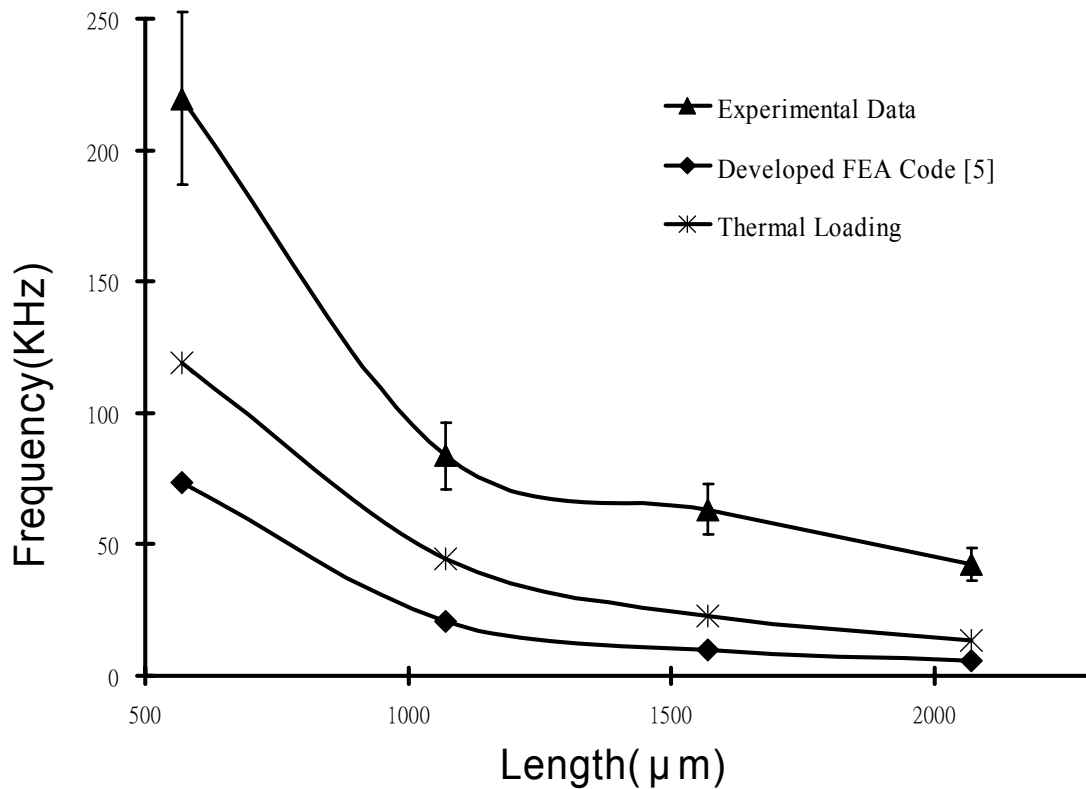
Figure 43: ANSYS thermal loading effects variation results compare to experimental data and FEA results

6.4: Effect of thickness and in-plane dimension variation

In the thermal cycling simulation, the dimensional variation was not considered. In this part of the study, both dimensional variation (15%) and shape change due to residual stresses generated by thermal cycling were considered. The results are shown in Figure 44. The resultant frequencies can be increased to the range of 161 KHz to 22 KHz, but they are still below the experimentally observed rage, 219 KHz to 42 KHz.
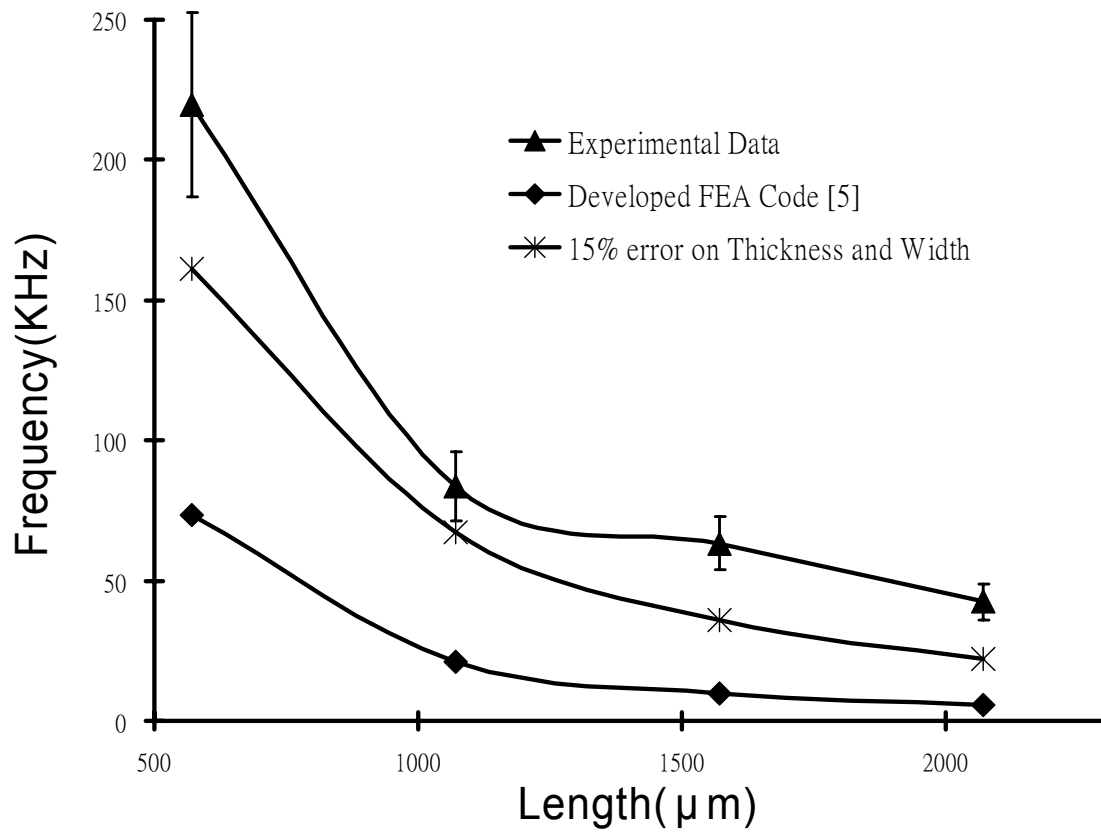
Figure 44: ANSYS thermal loading effects of thickness and in-plane dimension variation results compare to experimental data and FEA results

Chapter 7

Discussion

One possible reason for the underestimation of the ANSYS simulations might be due to the fact that the various intrinsic stresses were not considered in the simulation. At this point, ANSYS does not have the capability to simulate the residual stresses induce by the intrinsic stress

Another possible reason for the underestimation of ANSYS simulation is that the current simulation has not taken into consideration of the surrounding support for the membrane structure. In the current simulation, the support was simulated as clamped boundary condition. How much this boundary condition deviates from the actual support is uncertain at this point. In addition, the thermal cycling simulation used in the current study could also contribute to some errors. In the current simulation, all layers were subjected to the same thermal cycling at the same time. However, in the actual micro-fabrication processes, different layers were formed in sequences and in different temperatures. However, in this study, all layers were created in the preprocessing which is different from the real fabrication conditions.

Chapter 8

Conclusion

In this study, numerical simulation with ANSYS was used to gain insights into the dynamic responses of thin membrane structures. Specifically, the effects of dimensional variations and shape changes due to residual stress on the fundamental frequencies of the structures were examined and summarized below:

The specific conclusions drawn from this study are the following.

- Increase of thickness and decrease of in-plane dimensions increase the resonance frequencies.

- A 15% variation of thickness and in-plane dimensions as deemed reasonable from the practical point of view still could not bring up the predicted frequencies, which are in the range of 119 KHz ~ 9 KHz, within the experimentally observed range, which are in the range of 219 KHz ~ 42 KHz.

- Membranes with distorted shapes have high frequencies than the flat ones.

- The membrane with the domed shape has the highest frequency compared to other shapes the same size and out-of-plane displacement, but multi-curvatures.

- Thermal cycling was used to simulate the residual stress and the corresponding shape change. In this simulation, the structure was subjected to 25-1000-25° C thermal cycling and the resultant deformed shape was then used as an input for the subsequent dynamic analysis.

- The deformed shape obtained from thermal cycling simulation would still underestimate the frequencies quite significantly.

- With a combination of dimensional variation and shape change due to the simulated residual stress, the predicted frequencies, which are in range of 161 KHZ ~ 22 KHz, could be brought closer to the experimentally observed values, which are in the range of 219 KHZ ~ 42 KHz.

- Quantitative evaluation of the contribution from residual stress requires further study on the sources and realistic simulation of residual stresses.

References:

[1] W Fang and J A Wickert, 1996, "Determining mean and gradient residual stresses in thin films using micromachined cantilevers," *J.Micronech. Microeng*, 6, 301-309

[2] Lin SC H and Pugacz-Murasziewicz I, 1972, "Local stress measurement in thin termal Sio2 films on Si substrates," *J. Appl. Phys.* 43, 119-125

[3] Kiesewetter L, Zhang J-M, Houdeau D, and Steckenborn A, 1992, "Determination of Young's moduli of micromechanical thin films using the resonance method," *Sensors and Actors,* A 35, 153-159

[4] H. S. Choi, J. L. Ding, A. Bandyopadhyay, M. J. Anderson, and S. Bose, 2007, "Size effects on the performance of piezoelectric micromachined ultrasonic transducers (pMUTs) with large length/width aspect ratio," (submitted)

[5] H. S. Choi, J. L. Ding, A. Bandyopadhyay, and S. Bose, 2007, "Finite element analysis of piezoelectric thin film membrane structures," IEEE *Trans. Ultrason., Ferroelect., Freq. Contr.* (to appear).

[6] T. Myers, P. Banerjee, S. Bose, and A. Bandyopadhyay, "Layered lead zirconate titanate and lanthanum-doped lead zirconate titanate ceramic thin films," *J. Mater. Res.,*vol. 17, no. 9, pp. 2379-2385, Sep. 2002.

[7] H. S. Choi, J. L. Ding, A. Bandyopadhyay, M. J. Anderson, and S. Bose, 2007, " Length/width aspect ratio effect on the performance of piezoelectric micromachined ultrasonic transducers (pMUTs)," (submitted)

[8] J. N. Reddy, "On laminated composite plates with integrated sensors and actuators," *Eng. Struct.,* vol. 21, pp. 568-593, 1999.

[9] J. N. Reddy, *Mechanics of laminated composite plates and shells: Theory and Analysis*, Boca Raton, FL: CRC Press, 2004.

[10] J. Baborowski, P. Muralt, N. Ledermann, S. Petitgrand, A. Bosseboeuf, N. Setter, and Ph. Gaucher, "PZT coated membrane structures for micromachined ultrasonic transducers," in Proc. 13th *IEEE Int. Symp. Appl. Ferroelectric.,* 2002, pp. 483-486.

[11] P. Muralt, A. Kholkin, M. Kohli, and T. Maeder, "Piezoelectric actuation of PZT thin-film diaphragms at static and resonant conditions," *Sens. Actuators A,* vol. 53, pp. 398-404, 1996.

[12] ANSYS help

[13] Shawn J. Cunningham, Wan Suwito, and David T. Read, 1995, "TENSILE TESTING OF EPITAXIAL SILICON FILMS,*" The 8th International Conference on Solid-State Sensors and Actuators, and Eurosensors IX Stockholm, Sweden*, June, P.25-29.

[14] D. A. P. Bulla and J. D. Love, 2005, "Thickness-dependent stress in plasma-deposited silicon dioxide films," *JOURNAL OF APPLIED PHYSICS* **97**, 084912

[15] Kenneth G. KreiderU, Greg Gillen, 2000, "High temperature materials for thin-film thermocouples on silicon wafers," *Thin Solid Films*, 376, P.32-37

[16] S Mall, 2002, "Integrity of graphite/epoxy laminate embedded with piezoelectric sensor/actuator under monotonic and fatigue loads," *INSTITUTE OF PHYSICS Smart Mater. Struct.* 11, P.527–533

[17] H.D. Espinosa and B.C. Prorok, 2001, "Effects of Film Thickness on the Yielding Behavior of Polycrystalline Gold Films" *Accepted in the Materials Research Society Symposium Proceedings, vol. 695*

[18] Pietrzakoi, M., 2001"Active Damping of Beams by Piezoelectric System: Effect of Bonding Layer Properties," *Int. J. Solids and Structures,* Vol. 38, pp 7885~7897

[19] Sengupta, S.S., Park, S.M.et al., 1998, "Origins and evolution of stress Development in SolGel Derived Thin Layers and Multi deposited Coatingsd of Lead Titanata," *J. Appl. Phys.*, Vol. 83, No. 4, pp.2291~2296

[20] Okuyama, M., 2001,"Electronic devices using the ferroelectric thin film," *T. IEE Fapan,* Vol. 121_E, pp. 537~541. (in Japan)

[21] Thomas C. Hodge, Sue Ann Bidstrup-Allen, and Paul A. Kohl, 1997, " Stresses in Thin Film Metallization," *IEEE TRANSACTIONS ON COMPONENTS, PACKAGING, AND MANUFACTURING TECHNOLOGY*, PART A, VOL. 20, NO. 2

[22]Hutton, Fundamental of finite element analysis. 1st Ed.

[23] Ohring, M. Materials Science of Thin Films Deposition and Structure. 2nd Ed

[24] Gere, J. and Blech, I., J. *Applied Physic*, 1984;55:2874

[25] Boresi, A.P. and Chong, K.P., *Elasticity in Engineering Mechanics*, 2nd Ed., John Wiley & Sons, Inc., 2000

[26] Koch, R. The Intrinsic Stress of Polycrystalline and epitaxial thin metal films, *Journals of Physics Condensed Matter, Vol.6, 1994, 9519-9550*

[27] R.W. Hoffman, *Thin Solid Films*, 34, 185(1976)

[28] Klockholm, E and Berry, B.s., 1968," Intrinsic stress in evaporated metal films," *J Electrochem. Soc.,* 115:823

[29] Chaundri, P., 1973, "Grain growth and stress relief in thin film, *Journal of Vacuum Science and Technology,* 9, 520

[30] Zhang, X., Ghodssi, R., Chen, K.-S., Ayon, A., and Spearing, S., Residual stress characterization of thick PECVD TEO film for power MEMS application, *Solid-State Sensor and Actuator Workshop,* Hilton-Head, SC, June, 2002

[31] Mehrdad N. Ghasemi, Nejhad, Chiling Pan, Hongwei Feng, 2003, 'Intrinsic strain modeling and residual stress analysis for thin-film processing of layered structure,' *Journal of Electronic Packaging*, March 2003, Vol. 125, 4-17

[32] Seungmock Lee, Jong-Min Kim, and Young-Eui Shin, 2006, "The infulences of residual stress on the frequency of ultrasonic transducers with composite membrane structure," *J, of Mechanical Science and Technology (KSME Int. J.),* Vol.20, No.1, 76~84

Appendix1:

ANSYS program used to generate solid model

```
/PREP7
ET,1,SOLID45 % Element type
BLOCK,0.000535,-0.000535,-0.0000032,-0.0000014,0.000535,-0.000535, % Create a
BLOCK,0.000535,-0.000535,-0.0000014,-0.0000012,0.000535,-0.000535,
BLOCK,0.000535,-0.000535,-0.0000012,-0.0000010,0.000535,-0.000535,
BLOCK,0.000535,-0.000535,-0.0000010,-0.0000002,0.000535,-0.000535,
BLOCK,0.000535,-0.000535,-0.0000002,0.0000000,0.000535,-0.000535,
FLST,2,5,6,ORDE,2
FITEM,2,1
FITEM,2,-5
VGLUE,P51X
/input,menust,tmp,',,,,,,,,,,,,,,,,,,,1
WPSTYLE,,,,,,,,,0
MPTEMP,,,,,,,,,
MPTEMP,1,0
MPDATA,EX,1,,125e9
MPDATA,PRXY,1,,0.278
TB,BISO,1,1,2,
TBTEMP,0
TBDATA,,501e6,1e-9,,,,
MPTEMP,,,,,,,,,
MPTEMP,1,0
MPDATA,DENS,1,,2330
MPTEMP,,,,,,,,,
MPTEMP,1,0
UIMP,1,REFT,,,25
MPDATA,ALPX,1,,4.2e-6
MPTEMP,,,,,,,,,
MPTEMP,1,0
MPDATA,EX,2,,75e9
MPDATA,PRXY,2,,0.17
TB,BISO,2,1,2,
TBTEMP,0
TBDATA,,0.2e9,1e-9,,,,
MPTEMP,,,,,,,,,
MPTEMP,1,0
MPDATA,DENS,2,,2200
MPTEMP,,,,,,,,,
MPTEMP,1,0
UIMP,2,REFT,,,25
MPDATA,ALPX,2,,7.0e-6
MPTEMP,,,,,,,,,
```

```
clc
clear
r=0.004; L=570e-6; Dive=9; B=L/2;
X=[-B,-B,B,B];
Z=[-B,B,-B,B];
for q=1:4
   P(q,1)=X(1,q);
   P(q,3)=Z(1,q);
end
xstart=-L/2;
xendpoint=L/2;
xmiddle=0;
xdowncenter=-(r^2-(L/2)^2)^0.5;
xdowncenter+r
format short g
syms x y
for N=1:11
   q=q+1;
   point=xstart+(L/10)*(N-1);
   S=(x-xmiddle)^2+(y-xdowncenter)^2-r^2;
   a=subs(solve(S,y),x,point);
   P(q,1)=point;
   P(q,2)=-a(1);
end
zstart=-L/2;
zendpoint=L/2;
zmiddle=0;
zdowncenter=-(r^2-(L/2)^2)^0.5;
zdowncenter+r
for N=1:11
   q=q+1;
   point=zstart+(L/10)*(N-1);
   if (point==0)
      q=q-1;
   else
      S=(x-zmiddle)^2+(y-zdowncenter)^2-r^2;
      a=subs(solve(S,y),x,point);
      P(q,3)=point;
      P(q,2)=-a(1);
   end
end
MAX=max(abs(P(:,2)))*1e6
for ww=1:21
   for w=1:3
      d=abs(P(ww,w));
      if (d<1e-17);
         P(ww,w)=0;
      end
   end
end
```